Competitive Hardening Dynamics in Viscoplastic Materials with Evolving Threshold Stress

Yo-Lun Yang[a]

[a]*Graduate Institute of Manufacturing Technology, National Taipei University of Technology, Taipei, Taiwan*

Abstract

Conventional viscoplasticity frameworks treat the threshold stress as either a material constant or a strain-driven quantity. Such treatments are inadequate when microstructural evolution — whether precipitation, phase transformation, or solute redistribution — proceeds concurrently with deformation on time scales comparable to the loading history. The present work formulates a thermodynamically admissible framework in which the threshold stress evolves autonomously with physical time through postulated microstructural kinetics, decoupled from accumulated strain; admissibility is verified through the Clausius–Duhem inequality on the mechanical dissipation channels, within Perzyna-type overstress viscoplasticity. Modified Armstrong–Frederick kinematic hardening with static recovery is incorporated, so that back stress develops only during active inelastic flow. The interaction between time-driven threshold evolution and strain-driven back-stress development partitions material-point response into three behavioural regimes: purely elastic, flow arrest — in which inelastic flow initiates and then ceases as the threshold overtakes the effective stress — and continuous flow. The classification is predictive: the load ratio and asymptotic threshold determine the regime a priori. Asymptotic stability of flow arrest is established by direct integration of the decoupled post-arrest evolution equations, with explicit decay timescales. The regime classification and arrest-stability result both extend to any monotonically non-decreasing, bounded threshold evolution (Proposition 2), separating the structural content from the specific first-order kinetics adopted here. Back-stress development is further shown to reduce time to arrest through a kinematic hardening acceleration effect. A structural no-go result establishes (Proposition 1) that within the constant-threshold Armstrong–Frederick class, no parameter choice reproduces both an independently measured saturation back stress and the long-time deceleration of inelastic strain observed in the creep histories; the time-evolving threshold is therefore necessary as an independent internal state variable for any material satisfying the two stated empirical conditions. The framework is calibrated on a representative viscoplastic system using the back-stress test, which furnishes independent measurements of inelastic strain and back stress; a single parameter set reproduces both.

Keywords: Viscoplasticity, Threshold stress evolution, Back stress, Kinematic hardening, Flow arrest, Asymptotic stability

1. Introduction

Suppose that a viscoplastic material is subjected to a stress at elevated temperature. The initial response is entirely elastic and the original shape is recovered on complete unloading. Under sustained loading, however, the total strain separates into three contributions: an instantaneous elastic part, a time-dependent reversible part termed anelasticity, and a permanent viscous part that does not recover [1, 2]. From a series of strain-relaxation and recovery experiments on polycrystalline materials, Sinha [3, 4] first demonstrated the systematic existence of this separation. Further observations of anelastic backflow during stress reductions in creep [5] and recent characterisations of yielding and anelasticity in metals [6] have substantiated the experimental basis. At the continuum scale, the introduction of an opposing internal stress, termed the back stress, allows the heterogeneous internal stresses generated by dislocation

Email address: y.yang@ntut.edu.tw (Yo-Lun Yang)

cell structures during primary creep [7–9] to be represented through a single volume-averaged quantity [10–12]. Established protocols for back-stress measurement — stress relaxation, incremental unloading, strain-transient-dip [13], and hysteresis-loop dissipation methods [14] — yield discrete values rather than continuous histories. The constitutive question, however, is whether the time-evolving threshold and the strain-driven back stress can be coupled within a single thermodynamically admissible framework that admits flow arrest as a distinct regime.

Various viscoplasticity frameworks have been developed to describe the inelastic response of metals at elevated temperature. The conventional treatment, following Perzyna [15] and Chaboche [16–18], takes the threshold stress at which inelastic flow initiates to be either a material constant or a function of accumulated plastic strain alone. Although this treatment provides an adequate description when the microstructure remains stable, it becomes insufficient when microstructural evolution — precipitation, phase transformation, solute clustering, or thermally activated recovery — proceeds concurrently with creep. A clear counterexample was provided by Meyer and Ahlström [19], who showed for pearlitic steel that accumulated plastic strain alone does not suffice to describe yield-surface evolution. In this direction, considerable progress has been made through phenomenological models for time-evolving strength in precipitation-hardened alloys: modified Kocks–Mecking–Estrin formalisms [22], unified internal-state-variable creep-ageing kinetics [23], and mechanism-based dispersion-controlled creep [24], together with precipitation-kinetics models supplying the microstructural driver [20, 21]. There remains, however, a structural limitation in this approach: each model postulates the threshold-evolution kinetics rather than deriving them from a general thermodynamic framework with autonomous internal-variable evolution, and so remains tied to specific alloy systems or to pre-specified mechanism choices. A further distinction concerns the manner in which those kinetics couple to the deformation. In strain-coupled threshold-evolution kinetics — as in Ho et al. [23], where the precipitate-radius rate is taken proportional to the rate of viscous strain — strength evolution halts whenever inelastic flow halts. Flow arrest, in which inelastic flow initiates and then ceases while microstructural strengthening continues under the resulting null-flow state, cannot arise in such formulations. The autonomous time-evolution adopted here, in which the threshold evolves with physical time independently of the mechanical state, admits arrest as a distinct regime; this kinematic distinction motivates the structural analysis of Section 3.

The internal-state-variable framework due to Coleman and Gurtin [29] has been successfully applied to viscoplasticity in subsequent decades, in particular to cyclic elasto-viscoplasticity [30] and to wide-temperature thermo-viscoplasticity [31]. In developing a constitutive equation within this framework, it is necessary to take into account the structural inadequacy of two standard treatments of the threshold stress. Firstly, a constant threshold cannot represent the cessation of inelastic flow that occurs when microstructural strengthening overtakes the local effective stress. Secondly, a strain-driven threshold, which evolves only in the presence of active strain, cannot represent arrest at all. A time-evolving threshold stress $\sigma_Y(t)$, coupled to an autonomously evolving microstructural state variable, provides the minimal framework that admits both flow arrest and the regime in which arrest competes with strain-driven hardening.

Lyapunov stability theory provides the standard framework for the analysis of solids with internal-variable dissipation [32–34]. In general, however, these treatments are confined to rate-independent plasticity, and the corresponding analysis has not been extended to the viscoplastic case in which the threshold itself evolves with physical time. It remains to examine the conditions under which the cessation of inelastic flow at the point where the evolving threshold overtakes the effective stress is stable against perturbations, and the manner in which the back stress and microstructural state continue to evolve under static recovery and microstructural kinetics after that point — questions that have not, to the author's knowledge, been formally analysed in the viscoplastic creep literature.

Central to the present work is a viscoplastic framework derived from first principles: Clausius–Duhem thermodynamic consistency, Perzyna-type overstress viscoplasticity, and modified Armstrong–Frederick kinematic hardening with static recovery. The threshold stress evolves autonomously with physical time through microstructural kinetics (time-driven hardening), while the back stress develops only during active inelastic flow (strain-driven hardening). The relative magnitudes of the applied stress, the initial threshold, and the asymptotic threshold determine the qualitative response: when the applied stress does not exceed the initial threshold, the response remains entirely elastic; when the stress lies between the initial and the asymptotic thresholds, inelastic flow initiates and then ceases as microstructural strengthening raises the threshold above the local stress, a regime here termed flow arrest; and when the applied stress exceeds even the asymptotic threshold, inelastic flow persists indefinitely. Asymptotic stability of flow arrest is established by direct integration of the decoupled post-arrest evolution equations, with explicit decay timescales τ_{rec} and τ_h identified for the back stress and the microstructural state variable. The regime classification and the stability result apply not only to the first-order exponential kinetics adopted in the calibration, but also to any monotone

bounded threshold kinetics (Proposition 2 of Section 3.4), separating structural content from kinetic content. Two further results follow from the analysis. A kinematic-hardening acceleration effect arises from the early response of the back stress relative to the gradual threshold evolution. A structural no-go result, formalised in Proposition 1 of Section 3.4, asserts that no constant-threshold model can reproduce the calibration outcome once an independent saturation back-stress measurement is fixed.

An empirical illustration is obtained by considering a representative viscoplastic system in which the time-evolving threshold is experimentally accessible. The illustration draws on the back-stress test [35], a measurement technique developed by the author: the loading phase supplies time-resolved inelastic-strain histories, and the post-unloading phase yields direct back-stress measurements, so that the two subsystems are calibrated against independent data. The back-stress test and the related creep and recovery test are shown schematically in Figure 1; experimental specifics are reported in Section 4.

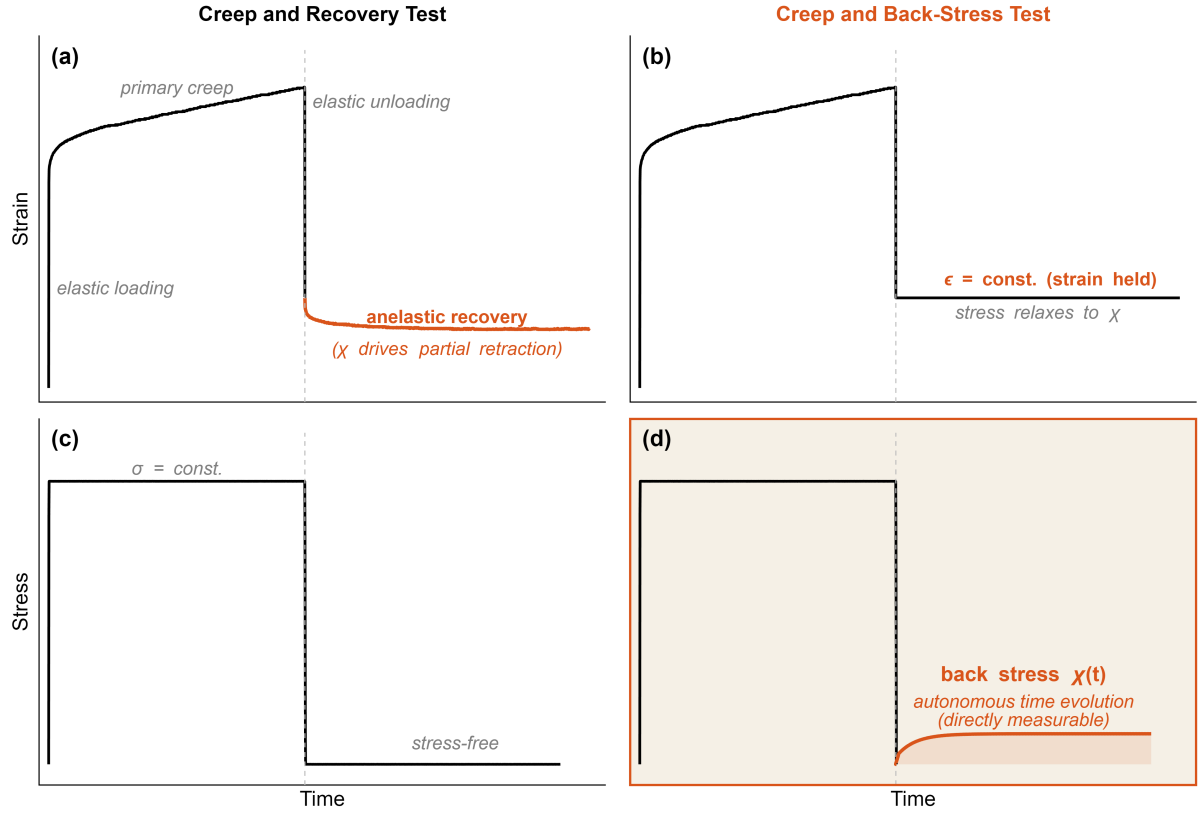

Figure 1: Schematic comparison of the creep and recovery test and the back-stress test; the two protocols measure inelastic strain and back-stress evolution respectively. (a) Strain response in the creep and recovery test: primary creep followed by anelastic recovery upon unloading; the back stress χ drives partial retraction. (b) Strain response in the back-stress test: strain held constant after unloading; stress relaxes to χ. (c) Stress protocol for the creep and recovery test: constant applied stress followed by stress-free recovery. (d) Stress protocol for the back-stress test: constant applied stress followed by strain-constrained hold, from which the autonomous back stress $\chi(t)$ is obtained.

2. Constitutive Framework

2.1. Thermodynamic Foundation

For a viscoplastic material exhibiting both recoverable and permanent inelastic deformation, the constitutive framework is developed within the thermodynamics of internal variables, following the internal state variable approach of Coleman and Gurtin [29]. The observable state is specified by the total strain tensor $\boldsymbol{\varepsilon}$ and the temperature T,

assumed constant throughout. The anelastic strain tensor $\boldsymbol{\varepsilon}^{\mathrm{an}}$ is introduced as an internal state variable associated with recoverable time-dependent deformation. A scalar microstructural state variable ξ, quantifying the degree of microstructural strengthening attained at a given instant, is introduced separately as a prescribed kinematic descriptor whose evolution is postulated in Section 2.2; thermodynamic admissibility of the resulting framework is verified in Section 2.4.

Under the assumption of small strains, the total strain decomposes additively as $\boldsymbol{\varepsilon} = \boldsymbol{\varepsilon}^{\mathrm{e}} + \boldsymbol{\varepsilon}^{\mathrm{in}}$, where $\boldsymbol{\varepsilon}^{\mathrm{e}}$ is the elastic strain and $\boldsymbol{\varepsilon}^{\mathrm{in}}$ the inelastic strain; the inelastic component is itself partitioned into recoverable and permanent parts, $\boldsymbol{\varepsilon}^{\mathrm{in}} = \boldsymbol{\varepsilon}^{\mathrm{an}} + \boldsymbol{\varepsilon}^{\mathrm{vis}}$. The anelastic component $\boldsymbol{\varepsilon}^{\mathrm{an}}$ stores recoverable elastic energy through an internal-stress field; upon unloading, this stored energy furnishes the driving force for time-dependent recovery. In crystalline metals this field is conventionally interpreted in terms of heterogeneous dislocation cell structures, but the formal role of $\boldsymbol{\varepsilon}^{\mathrm{an}}$ in the framework is independent of any particular microstructural realisation. The viscous component $\boldsymbol{\varepsilon}^{\mathrm{vis}}$ accumulates through irreversible processes — dislocation climb and annihilation in the crystalline-metal case — and is not recovered.

The specific Helmholtz free energy ψ is taken as the sum of elastic and anelastic contributions, $\psi = \psi^{\mathrm{e}}(\boldsymbol{\varepsilon}^{\mathrm{e}}) + \psi^{\mathrm{an}}(\boldsymbol{\varepsilon}^{\mathrm{an}})$. The viscous strain $\boldsymbol{\varepsilon}^{\mathrm{vis}}$ and the microstructural state variable ξ are absent from this ansatz by construction: in the Coleman–Noll procedure, only those internal variables whose evolution stores recoverable free energy enter ψ. The viscous strain is unrecoverably dissipated during inelastic flow, and ξ enters the framework as a prescribed kinematic descriptor coupled to the threshold (Section 2.2) rather than as a free-energy-storing internal variable; the anelastic strain $\boldsymbol{\varepsilon}^{\mathrm{an}}$, whose conjugate force defines the back stress (4), is the sole non-elastic contributor to ψ. Standard isotropic linear elasticity is adopted for $\psi^{\mathrm{e}} = \frac{1}{2\rho}\boldsymbol{\varepsilon}^{\mathrm{e}} : \mathbb{C} : \boldsymbol{\varepsilon}^{\mathrm{e}}$, with ρ the mass density and $\mathbb{C}$ the fourth-order elasticity tensor. The energy stored in dislocation cell wall stress fields takes the quadratic form

$$\psi^{\mathrm{an}} = \frac{c}{2\rho}\boldsymbol{\varepsilon}^{\mathrm{an}} : \boldsymbol{\varepsilon}^{\mathrm{an}} \tag{1}$$

with c [MPa] denoting the kinematic hardening modulus, which may be regarded as a measure of the stiffness of the internal dislocation structure.

Under isothermal conditions, the requirement of non-negative dissipation is expressed by the Clausius–Duhem inequality,

$$\mathcal{D} = \boldsymbol{\sigma} : \dot{\boldsymbol{\varepsilon}} - \rho\dot{\psi} \geq 0 \tag{2}$$

with $\boldsymbol{\sigma}$ the Cauchy stress tensor and the superposed dot the material time derivative. Expanding the free-energy rate through the strain decomposition and applying the standard Coleman–Noll argument — which requires the resulting inequality to hold for arbitrary elastic strain rates — yields the elastic constitutive relation

$$\boldsymbol{\sigma} = \rho\frac{\partial\psi}{\partial\boldsymbol{\varepsilon}^{\mathrm{e}}} = \mathbb{C} : \left(\boldsymbol{\varepsilon} - \boldsymbol{\varepsilon}^{\mathrm{in}}\right) \tag{3}$$

and identifies the thermodynamic force conjugate to the anelastic strain as the back-stress tensor,

$$\boldsymbol{\chi} = \rho\frac{\partial\psi}{\partial\boldsymbol{\varepsilon}^{\mathrm{an}}} = c\,\boldsymbol{\varepsilon}^{\mathrm{an}} \tag{4}$$

which may be interpreted physically as the internal stress generated by mobile dislocation structures; it opposes the applied stress and so reduces the effective driving force for continued flow. The reduced dissipation inequality follows as

$$\mathcal{D} = (\boldsymbol{\sigma} - \boldsymbol{\chi}) : \dot{\boldsymbol{\varepsilon}}^{\mathrm{an}} + \boldsymbol{\sigma} : \dot{\boldsymbol{\varepsilon}}^{\mathrm{vis}} \geq 0 \tag{5}$$

and all admissible evolution equations are required to satisfy this inequality.

2.2. Flow Rule and Threshold Evolution

The effective stress driving inelastic flow is obtained by subtracting the back stress from the deviatoric stress, giving

$$\boldsymbol{\Sigma} = \boldsymbol{\sigma}' - \boldsymbol{\chi} \tag{6}$$

where $\boldsymbol{\sigma}' = \boldsymbol{\sigma} - (1/3)(\mathrm{tr}\,\boldsymbol{\sigma})\mathbf{I}$ is the deviatoric stress and $\mathbf{I}$ the second-order identity tensor. Both $\boldsymbol{\varepsilon}^{\mathrm{an}}$ and $\boldsymbol{\varepsilon}^{\mathrm{vis}}$ are taken as individually deviatoric, consistent with the incompressible character of inelastic flow in metallic viscoplasticity; the total inelastic strain rate is accordingly incompressible ($\mathrm{tr}\,\dot{\boldsymbol{\varepsilon}}^{\mathrm{in}} = 0$), and the back stress $\boldsymbol{\chi} = c\,\boldsymbol{\varepsilon}^{\mathrm{an}}$ is purely deviatoric. The von Mises equivalent of the effective stress is

$$\Sigma_{\mathrm{eq}} = \sqrt{\frac{3}{2}\boldsymbol{\Sigma} : \boldsymbol{\Sigma}} \tag{7}$$

A yield function with time-dependent threshold is introduced as

$$f(\boldsymbol{\Sigma}, \sigma_Y) = \Sigma_{\mathrm{eq}} - \sigma_Y(\xi) \tag{8}$$

In contrast to classical formulations, in which the threshold is taken as constant or as a function of accumulated strain, here σ_Y evolves with time through the microstructural state variable ξ, giving

$$\sigma_Y(\xi) = \sigma_{Y0} + \Delta\sigma_Y \cdot \xi \tag{9}$$

where σ_{Y0} [MPa] is the initial threshold and $\Delta\sigma_Y$ [MPa] the threshold increment.

The kinetics of ξ are taken to follow first-order evolution,

$$\dot{\xi} = \frac{1}{\tau_h}(1 - \xi) \tag{10}$$

where τ_h [s] is the threshold time constant. The form (10) is postulated as a phenomenological constitutive choice; its thermodynamic admissibility is verified in Section 2.4, and Proposition 2 of Section 3.4 demonstrates that the regime classification and arrest-stability results are independent of this specific kinetic assumption. Direct integration of (10) gives $\xi(t) = 1 - e^{-t/\tau_h}$; substitution into (9) yields the explicit threshold history

$$\sigma_Y(t) = \sigma_{Y0} + \Delta\sigma_Y\left(1 - e^{-t/\tau_h}\right) \tag{11}$$

with asymptote $\sigma_{Y\infty} = \sigma_{Y0} + \Delta\sigma_Y$ and equivalent rate form $\dot{\sigma}_Y = (\sigma_{Y\infty} - \sigma_Y)/\tau_h$. It is this autonomous evolution that distinguishes the present formulation from conventional viscoplasticity: the threshold stress σ_Y increases with physical time regardless of whether flow is occurring, while the back stress $\boldsymbol{\chi}$ develops only during active inelastic deformation.

For associative viscoplasticity, the flow direction is taken normal to the yield surface, $\mathbf{N} = \partial f/\partial\boldsymbol{\sigma}$. Since $\boldsymbol{\Sigma}$ is already deviatoric, the chain rule through the effective stress reduces this to

$$\mathbf{N} = \frac{3}{2}\frac{\boldsymbol{\Sigma}}{\Sigma_{\mathrm{eq}}} \tag{12}$$

with the normalisation $\mathbf{N} : \mathbf{N} = 3/2$. The inelastic strain rate takes the form

$$\dot{\boldsymbol{\varepsilon}}^{\mathrm{in}} = \dot{p}\,\mathbf{N} \tag{13}$$

where the equivalent inelastic strain rate follows a power-law overstress relation,

$$\dot{p} = \frac{1}{\eta}\left\langle\frac{\Sigma_{\mathrm{eq}} - \sigma_Y(\xi)}{\sigma_0}\right\rangle^n \tag{14}$$

Here η [s] is the viscosity parameter, σ_0 [MPa] a reference stress, n the stress exponent, and $\langle\cdot\rangle$ the Macaulay bracket defined by

$$\langle x\rangle = \frac{x + |x|}{2} = \max(0, x) \tag{15}$$

Combining (12), (13), and (14), the complete flow rule becomes

$$\dot{\boldsymbol{\varepsilon}}^{\mathrm{in}} = \frac{1}{\eta}\left\langle \frac{\Sigma_{\mathrm{eq}} - \sigma_Y(\xi)}{\sigma_0} \right\rangle^{n} \frac{3}{2}\frac{\boldsymbol{\Sigma}}{\Sigma_{\mathrm{eq}}} \tag{16}$$

2.3. Back Stress Evolution with Static Recovery

The back stress is governed by a modified Armstrong–Frederick evolution equation [25–28] with an additional static recovery term,

$$\dot{\boldsymbol{\chi}} = c\,\dot{\boldsymbol{\varepsilon}}^{\mathrm{in}} - \kappa \boldsymbol{\chi}\,\dot{p} - \frac{\boldsymbol{\chi}}{\tau_{\mathrm{rec}}} \tag{17}$$

where κ is the dimensionless dynamic recovery coefficient and τ_{rec} [s] the static recovery time constant. On the right-hand side, the first term accounts for dislocation structure buildup during flow, the second for dynamic recovery through strain-induced annihilation, and the third for static recovery by thermal relaxation. Of these, the first two are active only during inelastic flow ($\dot{p} > 0$), whereas the static recovery term operates continuously, even in the absence of external loading. The static recovery term is the established Chaboche-tradition extension [25, 28] for representing thermal recovery at elevated temperature, and corresponds physically to thermally activated processes such as dislocation climb and cell coarsening.

The form of (17) may be motivated by a rheological model consisting of an internal Maxwell element through which the inelastic strain passes: an internal spring of stiffness c stores energy and generates back stress through $\boldsymbol{\chi} = c\,\boldsymbol{\varepsilon}^{\mathrm{an}}$ (4), while an internal dashpot of viscosity η_{int} permits viscous relaxation through $\dot{\boldsymbol{\varepsilon}}^{\mathrm{vis}}_{\mathrm{int}} = \boldsymbol{\chi}/\eta_{\mathrm{int}}$. Defining $\tau_{\mathrm{rec}} = \eta_{\mathrm{int}}/c$ and incorporating dynamic recovery during active flow recovers (17). The parameter τ_{rec} accordingly has a direct physical interpretation as the characteristic timescale over which back stress relaxes under zero external loading; the rheological arrangement is illustrated in Figure 2.

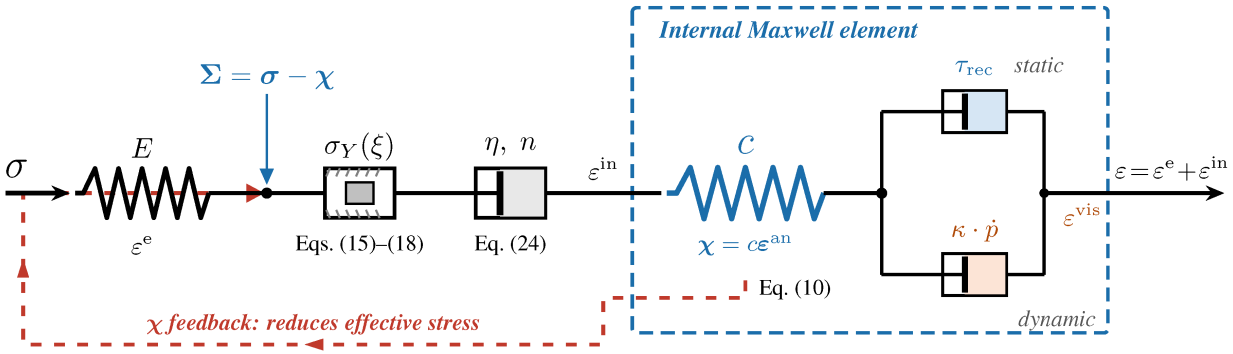

Figure 2: Rheological representation of the constitutive framework for viscoplastic materials with time-evolving threshold stress: elastic spring (E), time-evolving threshold element $\sigma_Y(\xi)$ driven by autonomous microstructural kinetics, viscoplastic dashpot (η, n), and internal Maxwell element for kinematic hardening with static (τ_{rec}) and dynamic ($\kappa \cdot \dot{p}$) recovery mechanisms. The effective stress $\boldsymbol{\Sigma} = \boldsymbol{\sigma}' - \boldsymbol{\chi}$ drives flow through the threshold.

Under multiaxial loading, the directional dependence of back-stress accumulation produces anisotropic recovery, in which directions with larger accumulated back stress recover more than those with less. The peak deformed and recovered strain states on the unit sphere under prescribed triaxial stress are shown in Figure 3.

Under constant strain rate proportional loading, the back stress approaches a steady-state value; in creep under constant stress, $\dot{p}$ varies with time, but the saturation value (18) below corresponds to the instantaneous equilibrium toward which χ tends at the prevailing strain rate. Setting $\dot{\boldsymbol{\chi}} = \mathbf{0}$ in the equivalent (von Mises) form of (17) and solving gives the equivalent saturation back stress

$$\chi_{\mathrm{sat}} = \frac{c\,\dot{p}}{\kappa\dot{p} + 1/\tau_{\mathrm{rec}}} = \frac{c}{\kappa + 1/(\dot{p}\tau_{\mathrm{rec}})} \tag{18}$$

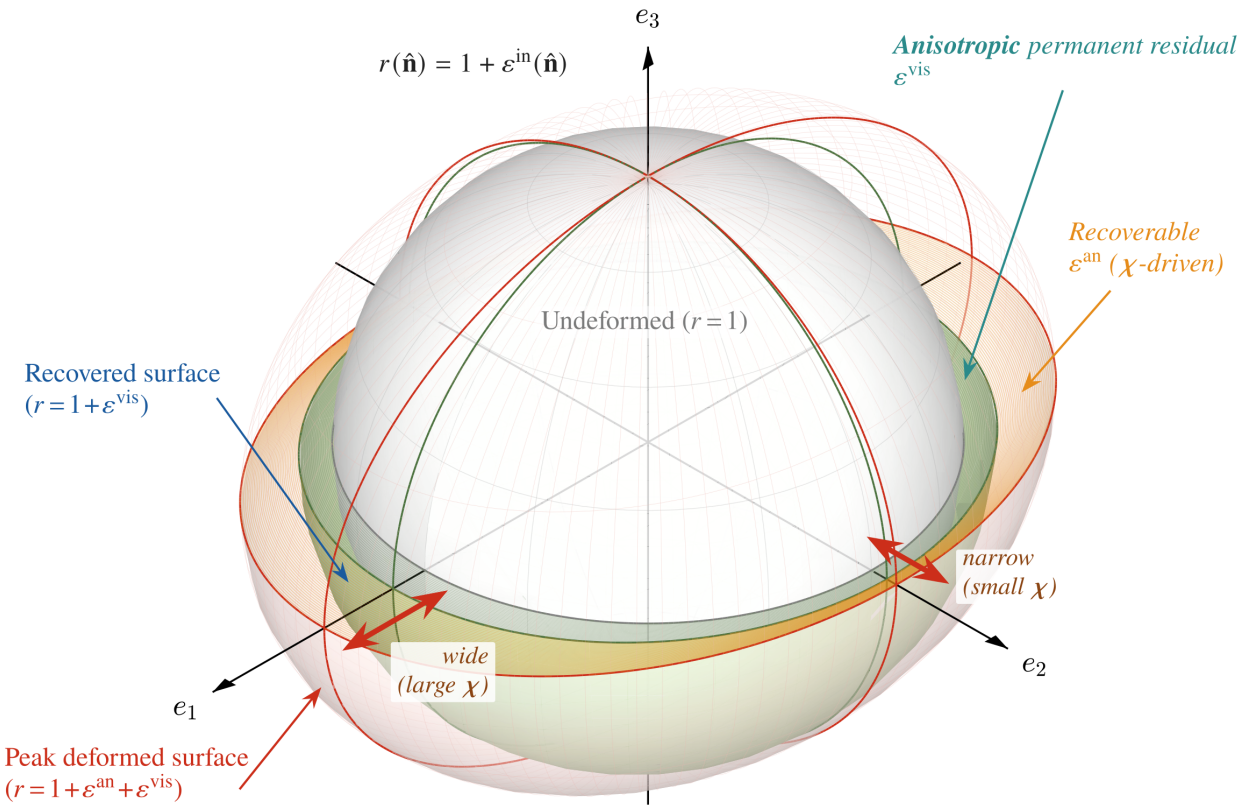

Figure 3: Anisotropic inelastic strain decomposition visualised on the unit sphere. The peak deformed surface (red) and recovered surface (green) are obtained by integrating the flow rule (16) and back-stress evolution (17) under prescribed triaxial stress ($\sigma_1 > \sigma_2 > \sigma_3$). Directions with larger accumulated back stress recover more, producing an irregular residual shape distinct from the deformed shape. Parameters chosen for visual clarity.

The saturation value depends on the strain rate solely through the dimensionless group $\dot{p}\tau_{\mathrm{rec}}$. When loading is fast ($\dot{p}\tau_{\mathrm{rec}} \gg 1$), dynamic recovery dominates and $\chi_{\mathrm{sat}} \to c/\kappa$; when loading is slow ($\dot{p}\tau_{\mathrm{rec}} \ll 1$), static recovery dominates and $\chi_{\mathrm{sat}} \to c\,\dot{p}\,\tau_{\mathrm{rec}}$. The crossover between these two regimes occurs at the characteristic rate $\dot{p}^* = 1/(\kappa\tau_{\mathrm{rec}})$; the saturation behaviour therefore spans continuously from the rate-independent limit to the fully viscous limit. Figure 4 shows $\chi_{\mathrm{sat}}/(c/\kappa)$ as a function of $\dot{p}\tau_{\mathrm{rec}}$.

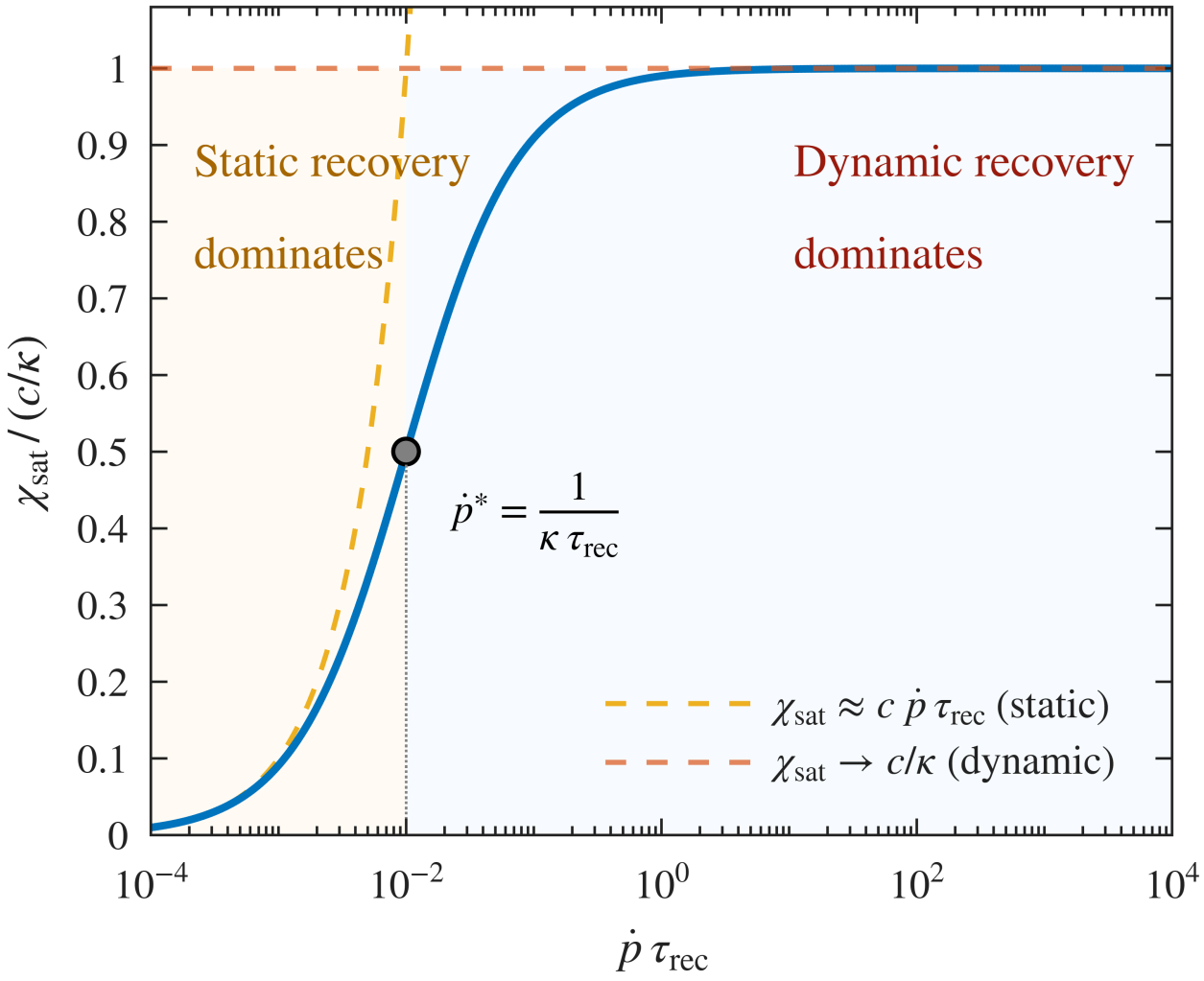

Figure 4: Normalised back-stress saturation $\chi_{\mathrm{sat}}/(c/\kappa)$ as a function of the dimensionless strain rate–recovery time product $\dot{p}\tau_{\mathrm{rec}}$, showing the transition from static-recovery-dominated ($\chi_{\mathrm{sat}} \approx c\dot{p}\tau_{\mathrm{rec}}$) to dynamic-recovery-dominated ($\chi_{\mathrm{sat}} \to c/\kappa$) regimes. The crossover occurs at $\dot{p}^* = 1/(\kappa\tau_{\mathrm{rec}})$.

The partition of the inelastic strain rate into anelastic and viscous parts follows from (4) and (17). Differentiating $\boldsymbol{\chi} = c\,\boldsymbol{\varepsilon}^{\mathrm{an}}$ in time gives $\dot{\boldsymbol{\chi}} = c\,\dot{\boldsymbol{\varepsilon}}^{\mathrm{an}}$, and substituting (17) yields the anelastic strain rate

$$\dot{\boldsymbol{\varepsilon}}^{\mathrm{an}} = \frac{1}{c}\dot{\boldsymbol{\chi}} = \dot{\boldsymbol{\varepsilon}}^{\mathrm{in}} - \frac{\kappa}{c}\boldsymbol{\chi}\,\dot{p} - \frac{\boldsymbol{\chi}}{c\,\tau_{\mathrm{rec}}} \tag{19}$$

Since $\dot{\boldsymbol{\varepsilon}}^{\mathrm{in}} = \dot{\boldsymbol{\varepsilon}}^{\mathrm{an}} + \dot{\boldsymbol{\varepsilon}}^{\mathrm{vis}}$, the viscous strain rate is

$$\dot{\boldsymbol{\varepsilon}}^{\mathrm{vis}} = \frac{\kappa}{c}\boldsymbol{\chi}\,\dot{p} + \frac{\boldsymbol{\chi}}{c\,\tau_{\mathrm{rec}}} \tag{20}$$

The viscous strain accordingly accumulates through two mechanisms, namely dynamic conversion during active

flow and static conversion by thermal relaxation.

When the stress lies below the threshold ($\Sigma_{\mathrm{eq}} < \sigma_Y$), the Macaulay bracket gives $\dot{p} = 0$ and (17) reduces to $\dot{\boldsymbol{\chi}} = -\boldsymbol{\chi}/\tau_{\mathrm{rec}}$, integrating to $\boldsymbol{\chi}(t) = \boldsymbol{\chi}_0 \exp(-t/\tau_{\mathrm{rec}})$; (19) and (20) reduce correspondingly, giving $\dot{\boldsymbol{\varepsilon}}^{\mathrm{an}} = -\boldsymbol{\chi}/(c\,\tau_{\mathrm{rec}})$ and $\dot{\boldsymbol{\varepsilon}}^{\mathrm{vis}} = \boldsymbol{\chi}/(c\,\tau_{\mathrm{rec}})$. The anelastic strain therefore decays exponentially toward zero while the viscous strain accumulates the permanent component. This exponential recovery is the mechanism responsible for the creep recovery observed experimentally in strain relaxation and recovery tests [3, 4].

2.4. Thermodynamic Consistency

The constitutive model defined by Eqs. (16), (17), (19), (20), and (10) satisfies the Clausius–Duhem inequality for all admissible processes. Starting from the reduced dissipation (5), and noting that $\dot{\boldsymbol{\varepsilon}}^{\mathrm{an}}$ and $\dot{\boldsymbol{\varepsilon}}^{\mathrm{vis}}$ are traceless, the dissipation may be expressed in terms of deviatoric quantities as

$$\mathcal{D} = \boldsymbol{\Sigma} : \dot{\boldsymbol{\varepsilon}}^{\mathrm{an}} + \boldsymbol{\sigma}' : \dot{\boldsymbol{\varepsilon}}^{\mathrm{vis}} \tag{21}$$

Substituting the anelastic strain rate (19) and the viscous strain rate (20) into (21), using the flow rule $\dot{\boldsymbol{\varepsilon}}^{\mathrm{in}} = \dot{p}\,\mathbf{N}$ with $\mathbf{N} = (3/2)\boldsymbol{\Sigma}/\Sigma_{\mathrm{eq}}$, the identity $\boldsymbol{\Sigma} : \boldsymbol{\Sigma} = (2/3)\Sigma_{\mathrm{eq}}^2$, and the relation $\boldsymbol{\sigma}' : \boldsymbol{\chi} - \boldsymbol{\Sigma} : \boldsymbol{\chi} = \|\boldsymbol{\chi}\|^2$ that follows from $\boldsymbol{\sigma}' - \boldsymbol{\Sigma} = \boldsymbol{\chi}$, the mechanical dissipation simplifies to

$$\mathcal{D}_{\mathrm{mech}} = \Sigma_{\mathrm{eq}}\,\dot{p} + \frac{\kappa}{c}\|\boldsymbol{\chi}\|^2\dot{p} + \frac{\|\boldsymbol{\chi}\|^2}{c\,\tau_{\mathrm{rec}}} \tag{22}$$

Each term on the right-hand side is non-negative, since $\Sigma_{\mathrm{eq}} \geq 0$ by definition, $\dot{p} \geq 0$ from the Macaulay bracket, κ, c, $\tau_{\mathrm{rec}} > 0$ as material parameters, and $\|\boldsymbol{\chi}\|^2 \geq 0$. It follows that

$$\mathcal{D}_{\mathrm{mech}} \geq 0 \quad \text{for all admissible processes} \tag{23}$$

The mechanical dissipation may be decomposed into three contributions,

$$\mathcal{D}_{\mathrm{mech}} = \mathcal{D}_{\mathrm{flow}} + \mathcal{D}_{\mathrm{dyn}} + \mathcal{D}_{\mathrm{stat}} \tag{24}$$

in which $\mathcal{D}_{\mathrm{flow}} = \Sigma_{\mathrm{eq}}\,\dot{p}$ is the viscous resistance to inelastic flow, $\mathcal{D}_{\mathrm{dyn}} = (\kappa/c)\|\boldsymbol{\chi}\|^2\dot{p}$ the dissipation associated with dynamic recovery, and $\mathcal{D}_{\mathrm{stat}} = \|\boldsymbol{\chi}\|^2/(c\,\tau_{\mathrm{rec}})$ the static recovery dissipation. Of these, $\mathcal{D}_{\mathrm{stat}}$ is of particular interest: it remains positive whenever $\boldsymbol{\chi} \neq \mathbf{0}$, regardless of whether inelastic flow is occurring, so that energy is dissipated by thermal relaxation of dislocation structures even in the absence of mechanical loading. Classical kinematic hardening models, which lack a static recovery mechanism, do not exhibit this behaviour.

The thermodynamic treatment of the threshold stress $\sigma_Y(t)$ deserves separate comment. Unlike the back stress — which evolves only during active flow — the threshold increases continuously with time irrespective of the mechanical loading state; this time-driven evolution is accommodated through the microstructural state variable ξ introduced in Section 2.1, which enters the framework as a prescribed kinematic descriptor with postulated kinetics (10), coupled to the threshold through (9). Because ξ does not contribute to the Helmholtz free energy, it carries no associated stored-energy term and is absent from the mechanical dissipation (24); thermodynamic admissibility of the coupled framework follows directly from $\mathcal{D}_{\mathrm{mech}} \geq 0$.

The first-order kinetics (10) are written in general terms that do not presuppose a particular microstructural mechanism. The autonomous time-evolution adopted here has precedent in the precipitation-strengthened-superalloy literature [24], where microstructural strengthening variables are coupled directly to creep deformation. For precipitation-hardening alloys, the state variable ξ admits a direct physical interpretation in terms of precipitate evolution: Lifshitz–Slyozov–Wagner coarsening gives a normalised precipitate state evolving as $\bar{r}_n^3 - \bar{r}_{n,0}^3 = K_{\mathrm{LSW}}\,t$, and the first-order kinetics adopted in (10) is a linearised approximation valid during the initial hardening transient, before significant coarsening sets in; the regime in which strengthening saturates and reverses would require higher-order kinetic descriptions.

The complete system comprises the elasticity relation (3), back-stress definition (4), threshold–microstructure coupling (9), evolution kinetics (10), flow rule (16), back-stress evolution (17), and strain partition (19)–(20). The material parameters governing the framework are listed in Table 1.

Table 1: Material parameters of the constitutive framework.

Symbol	Units	Physical Meaning
λ, μ	MPa	Lamé elastic constants
η	s	Viscous flow resistance
n	—	Stress exponent
σ_0	MPa	Reference stress
c	MPa	Kinematic hardening modulus
κ	—	Dynamic recovery coefficient
τ_{rec}	s	Static recovery time
σ_{Y0}	MPa	Initial threshold
$\Delta\sigma_Y$	MPa	Threshold increment
τ_h	s	Threshold time constant

The framework reduces to classical Armstrong–Frederick kinematic hardening when $\tau_{\text{rec}} \to \infty$ (no static recovery) and $\xi = 0$, $\sigma_Y = \sigma_{Y0}$ (no threshold evolution).

Although the individual equations in the preceding framework are drawn from established viscoplasticity theory, their coupling — specifically, the autonomous time evolution of σ_Y competing with the strain-driven evolution of $\boldsymbol{\chi}$ — gives rise to three distinct behavioural regimes, including flow arrest (defined in Section 1) in which inelastic flow initiates but subsequently ceases. These phenomena, which have not been analysed in the existing literature, are characterised in Section 3.

3. Competitive Hardening Dynamics

Within the constitutive framework of Section 2, two hardening mechanisms differ in their time dependence. The threshold stress $\sigma_Y(t)$ evolves autonomously with physical time, whereas the back stress $\boldsymbol{\chi}$ grows only during active inelastic flow, though static recovery may diminish it regardless of the flow state. The long-time deformation behaviour is accordingly governed by the competition between these two mechanisms.

3.1. Regime Classification

Under constant applied stress the back stress remains aligned with the deviatoric stress throughout monotonic loading, and the condition for inelastic flow, $\Sigma_{\text{eq}} > \sigma_Y$, reduces to a comparison between a scalar driving force and the total resistance to flow. The driving force is the applied stress invariant $\mathcal{F}(t) = \sigma_{\text{eq}}(t) \equiv \sqrt{\frac{3}{2}\,\boldsymbol{\sigma}'(t) : \boldsymbol{\sigma}'(t)}$, the von Mises equivalent of the deviatoric stress. (The double-bar symbol $\|\cdot\|$ is reserved throughout this work for the Frobenius norm, as in $\|\boldsymbol{\chi}\|^2 = \boldsymbol{\chi} : \boldsymbol{\chi}$ used in Section 2.4; equivalent stresses are denoted with the subscript eq.) Under constant applied loading, $\mathcal{F}$ remains constant or changes only through stress redistribution. The total resistance is the sum of all mechanisms opposing flow, $\mathcal{R}(t) = \sigma_Y(t) + \chi_{\text{eq}}(t)$ with $\chi_{\text{eq}} = \sqrt{\frac{3}{2}\boldsymbol{\chi} : \boldsymbol{\chi}}$, and inelastic flow occurs precisely when $\mathcal{F} > \mathcal{R}$.

The two components of $\mathcal{R}$ evolve at different rates. The threshold rate $\dot{\sigma}_Y = (\Delta\sigma_Y/\tau_h)\, e^{-t/\tau_h} \geq 0$, obtained by differentiating (11), is always active; the back-stress rate $\dot{\chi}_{\text{eq}} = (3/2)(\boldsymbol{\chi} : \dot{\boldsymbol{\chi}})/\chi_{\text{eq}}$, obtained from (17), is active only when $\dot{p} > 0$. The threshold stress therefore increases monotonically regardless of the mechanical loading state, approaching $\sigma_{Y\infty} = \sigma_{Y0} + \Delta\sigma_Y$ asymptotically. The back stress, in contrast, evolves only during active flow; if flow ceases, it either remains constant (when $\tau_{\text{rec}} \to \infty$) or decays through static recovery.

The coupling between these two mechanisms produces a competition between time-driven hardening — $\sigma_Y(t)$ increasing continuously — and strain-driven hardening, in which $\boldsymbol{\chi}$ grows only during flow. Three long-time outcomes are then possible. If the resistance exceeds the driving force from the outset, no flow occurs (Regime I); if the resistance catches up at a finite time t^*, flow arrest takes place (Regime II); and if the driving force always exceeds the resistance, flow continues indefinitely (Regime III).

Two dimensionless parameters characterise the long-time behaviour. The load ratio

$$\Lambda = \frac{\sigma_{\mathrm{eq}}}{\sigma_{Y0}} \tag{25}$$

compares the applied stress invariant σ_{eq} to the initial yield resistance, and the hardening capacity

$$\Gamma = \frac{\Delta\sigma_Y}{\sigma_{Y0}} \tag{26}$$

is the fractional increase in threshold stress from the initial to the asymptotic state.

To complete the description, two further dimensionless groups are introduced. The dimensionless time is

$$\Pi_t = \frac{t}{\tau_h} \tag{27}$$

and the back-stress saturation ratio is

$$\Pi_\chi = \frac{\chi_{\mathrm{sat}}}{\sigma_{Y0}} \tag{28}$$

in which $\chi_{\mathrm{sat}} = c/\kappa$ is the upper bound of the saturation back stress, corresponding to the dynamic-recovery-dominated limit of (18).

In terms of these parameters, and writing the equivalent back-stress evolution under monotonic proportional loading with static recovery neglected during the flow phase — valid when $\dot{p}\,\tau_{\mathrm{rec}} \gg 1$, the condition that also underlies the upper-bound choice $\chi_{\mathrm{sat}} = c/\kappa$ in (28) and the long-time analysis of Section 3.2 — so that $\chi_{\mathrm{eq}}(p) = (c/\kappa)[1 - \exp(-\kappa p)]$, the flow condition at any instant becomes

$$\Lambda > 1 + \Gamma\left(1 - e^{-\Pi_t}\right) + \Pi_\chi\left(1 - e^{-\kappa p}\right) \tag{29}$$

The two exponential terms on the right-hand side give the current fractional evolution of threshold stress and back stress respectively. For different values of Λ and Γ, the inequality (29) delineates three regimes. In Regime I ($\Lambda < 1$), the stress lies below the initial threshold and the response is purely elastic. In Regime II ($1 < \Lambda < 1 + \Gamma$), microstructural hardening arrests flow at a finite time. In Regime III ($\Lambda > 1 + \Gamma$), the stress exceeds the asymptotic threshold and flow continues indefinitely.

In the (Λ, Γ) parameter space the three regimes form a map that is of practical interest for process design. Regime II occupies a triangular region bounded by $\Lambda = 1$, $\Lambda = 1 + \Gamma$, and the positive Γ axis. For a given material (fixed Γ), the value of Λ determines whether arrest occurs; conversely, for a given loading condition, the hardening capacity Γ controls whether the flow can be arrested.

The regime boundaries stated above are necessary conditions that neglect the back-stress contribution. When kinematic hardening is included, the arrest regime expands, since the back stress provides additional resistance that reduces the effective driving force. The resulting acceleration of flow arrest is quantified in Section 3.3; the three-regime structure is displayed in Figure 5 as a phase map in the $(t/\tau_h, \Lambda)$ plane.

The gap between the two arrest boundaries in Figure 5 varies systematically with load ratio. Near the lower boundary ($\Lambda \to 1$), the brief flow duration limits back-stress accumulation, and the gap vanishes. As Λ increases through Regime II, the gap grows monotonically. Near the upper boundary ($\Lambda \to 1 + \Gamma$), the gap diverges: t_0^* grows without bound as the threshold approaches σ_{eq} asymptotically, while t^* remains finite because the back stress supplies a reserve bounded by $\chi_{\mathrm{sat}} = c/\kappa$. For the illustrative parameters shown, the back stress accelerates arrest by approximately $\Delta t^*/\tau_h \approx 0.3$ at $\Lambda = 1.25$.

Remark (degenerate case $\sigma_{Y0} = 0$). When the initial threshold vanishes, the dimensionless parameters Λ, Γ, and Π_χ defined in (25), (26), and (28) become undefined because each uses σ_{Y0} as the normalising stress. In this degenerate case the natural normalisation employs the asymptotic threshold $\sigma_{Y\infty} = \Delta\sigma_Y$, giving the reduced load ratio $\Lambda_\infty = \sigma_{\mathrm{eq}}/\sigma_{Y\infty}$, the reduced back-stress ratio $\Pi_{\chi,\infty} = \chi_{\mathrm{sat}}/\sigma_{Y\infty}$, and $\Gamma_\infty = 1$ by construction. The regime classification then simplifies to two cases — continuous flow ($\Lambda_\infty > 1$) and eventual arrest ($\Lambda_\infty < 1$) — with no purely elastic regime, since every nonzero stress exceeds the zero initial threshold. The arrest time (43) reduces to

$$\frac{t^*}{\tau_h} = -\ln\left(1 - \Lambda_\infty\right) \tag{30}$$

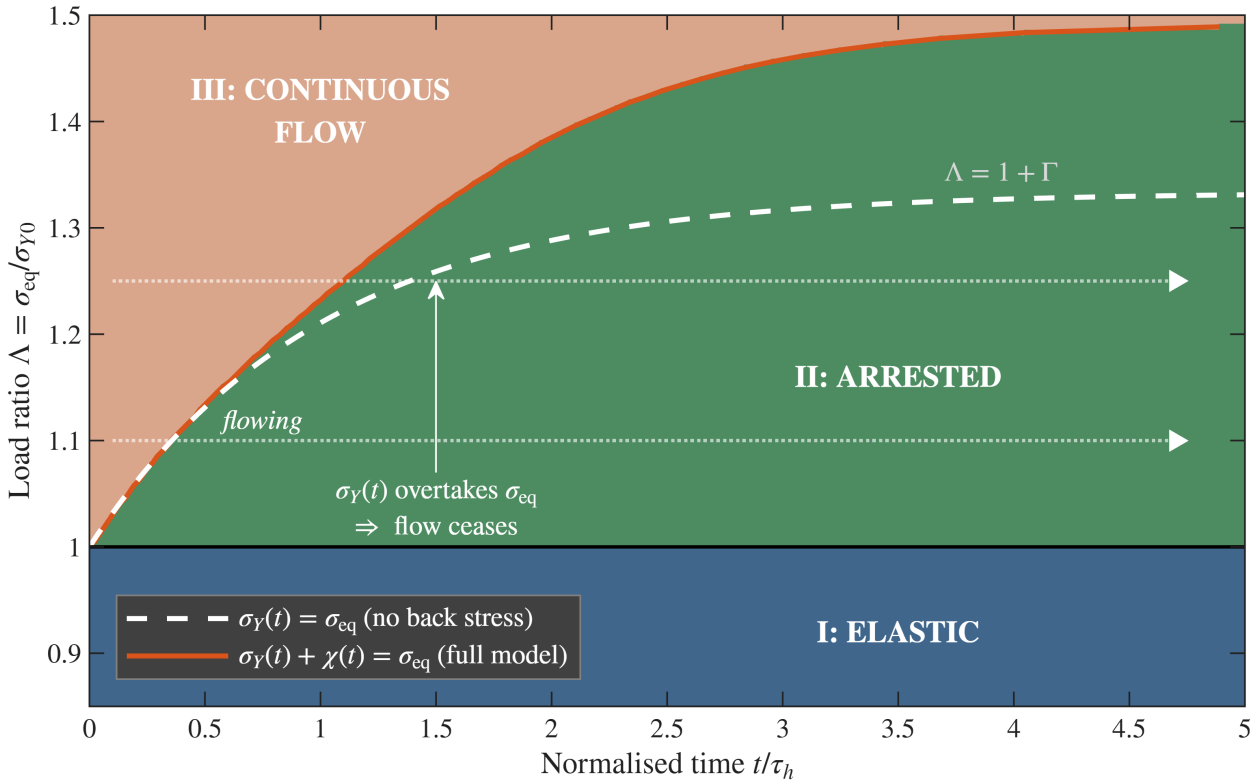

Figure 5: Theoretical phase map: the three behavioural regimes in the $(t/\tau_h, \Lambda)$ plane — elastic ($\Lambda < 1$, blue), arrested (green), and continuous-flow (coral). At early times, material in Regime II flows transiently before arrest (coral wedge). Solid red curve: arrest boundary from the full model, $\sigma_Y(t) + \chi_{eq}(t) = \sigma_{eq}$. White dashed curve: arrest boundary neglecting back stress, $\sigma_Y(t) = \sigma_{eq}$. The gap between the two boundaries corresponds to the acceleration effect discussed in Section 3.3; kinematic hardening reduces arrest time by providing immediate resistance that supplements the slower threshold evolution. Illustrative parameters with $\Pi_\chi = c/(\kappa\sigma_{Y0}) = 0.33$.

and all results of Sections 3.2–3.3 carry through with $\sigma_{Y\infty}$ replacing σ_{Y0} as the normalising stress. This case arises naturally in systems where the initial dislocation barrier is negligible, so that the entire flow resistance develops through microstructural evolution.

3.2. Stability of Flow Arrest

A natural question is whether flow arrest, once achieved, is permanent. Two distinct claims are established below. The first is *local irreversibility*: once the overstress vanishes, it cannot reopen, so the Macaulay bracket in the flow rule (14) remains pinned at zero and inelastic flow cannot resume. This is a kinematic statement about the sign of $\dot{f}$ at and after t^*, established by direct analysis of the overstress rate. The second is *asymptotic stability of the post-arrest equilibrium*: the internal variables $\boldsymbol{\chi}$ and ξ continue to evolve after arrest and converge to $\boldsymbol{\chi} = \mathbf{0}$, $\xi = 1$. The two subsystems decouple once flow ceases, and their convergence follows by direct integration of two first-order linear ODEs with explicit decay rates. The two claims are logically independent: the kinematic argument precludes resumption of flow without addressing the long-time evolution of $\boldsymbol{\chi}$ and ξ, while the integration argument characterises that evolution without itself precluding flow resumption.

Flow arrest occurs when the overstress vanishes with a non-positive rate of change, so that

$$f(t^*) = 0 \quad \text{and} \quad \dot{f}(t^*) \leq 0 \tag{31}$$

The first of these conditions marks the instant of arrest; the second precludes immediate resumption of flow.

To evaluate $\dot{f}$ at arrest, we differentiate the overstress function, giving

$$\dot{f} = \dot{\Sigma}_{\text{eq}} - \dot{\sigma}_Y \tag{32}$$

Under constant applied stress with an evolving back stress, the rate of effective stress follows from the chain rule as

$$\dot{\Sigma}_{\text{eq}} = \frac{\partial \Sigma_{\text{eq}}}{\partial \boldsymbol{\chi}} : \dot{\boldsymbol{\chi}} = -\frac{3}{2}\frac{\boldsymbol{\Sigma}}{\Sigma_{\text{eq}}} : \dot{\boldsymbol{\chi}} = -\mathbf{N} : \dot{\boldsymbol{\chi}} \tag{33}$$

The negative sign reflects the opposition between back stress and effective stress.

At the instant of arrest the viscoplastic multiplier $\dot{p} \to 0^+$ while remaining positive, the arrest being approached from active flow. Substituting into the back-stress evolution law (17) gives

$$\dot{\boldsymbol{\chi}}|_{\text{arrest}} = c\,\dot{p}\,\mathbf{N} - \kappa \boldsymbol{\chi}\dot{p} - \frac{\boldsymbol{\chi}}{\tau_{\text{rec}}} \to -\frac{\boldsymbol{\chi}}{\tau_{\text{rec}}} \quad \text{as } \dot{p} \to 0^+ \tag{34}$$

The rate of effective stress at arrest is therefore

$$\dot{\Sigma}_{\text{eq}}|_{\text{arrest}} = -\mathbf{N} : \left(-\frac{\boldsymbol{\chi}}{\tau_{\text{rec}}}\right) = \frac{\mathbf{N} : \boldsymbol{\chi}}{\tau_{\text{rec}}} \tag{35}$$

Under monotonic loading from virgin conditions, both $\mathbf{N}$ and $\boldsymbol{\chi}$ point in the direction of the applied deviatoric stress — $\mathbf{N}$ because it is the flow direction, and $\boldsymbol{\chi}$ because it accumulates along the flow direction during prior deformation — so that $\mathbf{N} : \boldsymbol{\chi} > 0$ and hence $\dot{\Sigma}_{\text{eq}}|_{\text{arrest}} > 0$. It follows that the effective stress *increases* at the instant of arrest as a consequence of back-stress relaxation.

At arrest ($t = t^*$), the overstress rate is obtained from (32) and (35), with the threshold rate $\dot{\sigma}_Y(t^*) = (\Delta\sigma_Y/\tau_h)\, e^{-t^*/\tau_h}$ from Section 3.1, as

$$\dot{f}\Big|_{t^*} = \dot{\Sigma}_{\text{eq}}\Big|_{t^*} - \dot{\sigma}_Y(t^*) = \frac{\mathbf{N} : \boldsymbol{\chi}}{\tau_{\text{rec}}} - \frac{\Delta\sigma_Y}{\tau_h} e^{-t^*/\tau_h} \tag{36}$$

In the arrest regime (II) we have $\sigma_Y(t^*) < \sigma_{Y\infty}$, which requires

$$e^{-t^*/\tau_h} > 0 \tag{37}$$

The threshold stress accordingly continues to increase after arrest. Although Σ_{eq} also increases through back-stress relaxation (35), the threshold increases at a faster rate, provided the static recovery timescale is sufficiently

large relative to the microstructural-evolution timescale. After arrest, the back stress decays exponentially through static recovery, $\chi_{\mathrm{eq}}(t) = \chi_{\mathrm{eq}}(t^*)\exp\left[-(t-t^*)/\tau_{\mathrm{rec}}\right]$, and the effective stress recovery rate is therefore bounded by $\chi_{\mathrm{eq}}(t^*)/\tau_{\mathrm{rec}}$, using the identity $\mathbf{N}:\boldsymbol{\chi} = \chi_{\mathrm{eq}}$ for proportional aligned loading. Arrest is strictly irreversible — in the sense that $\dot{f} \le 0$ for all $t > t^*$ — when the threshold growth rate exceeds this recovery rate at $t = t^*$, which requires

$$\frac{\tau_{\mathrm{rec}}}{\tau_h} > \frac{\chi_{\mathrm{eq}}(t^*)}{\Delta\sigma_Y\, e^{-t^*/\tau_h}} \tag{38}$$

For parameter combinations in which $\tau_{\mathrm{rec}} \gg \tau_h$, condition (38) is automatically satisfied. The calibrated instance of Section 4 falls in this regime. The threshold growth rate at arrest is given by

$$\dot{\sigma}_Y(t^*) = \frac{\sigma_{Y\infty} - \sigma_Y(t^*)}{\tau_h} > 0 \tag{39}$$

In the absence of static recovery, both the stress and the back-stress distributions become time-independent after arrest. Even when τ_{rec} is finite, the total stress $\boldsymbol{\sigma}$ remains frozen because the elastic strain compensates for back-stress relaxation through (3). The final stress state consequently depends on the arrest time t^* rather than on asymptotic values, and process design must account for the transient evolution, not merely for the steady-state parameters.

The preceding argument establishes local irreversibility: $\dot{f} \le 0$ at and after t^*, so flow does not resume. It does not, however, address the long-time behaviour of the internal variables $\boldsymbol{\chi}$ and ξ, which continue to evolve through static recovery and microstructural kinetics. Both subsystems decouple after arrest, and their convergence follows by direct integration. With $\dot{p} = 0$, the back-stress evolution (17) reduces to $\dot{\boldsymbol{\chi}} = -\boldsymbol{\chi}/\tau_{\mathrm{rec}}$, integrating to $\boldsymbol{\chi}(t) = \boldsymbol{\chi}(t^*)\exp[-(t-t^*)/\tau_{\mathrm{rec}}]$ and converging to $\boldsymbol{\chi} = \mathbf{0}$ with decay rate $1/\tau_{\mathrm{rec}}$. The microstructural state ξ continues to evolve according to (10) independently of the flow, integrating to $\xi(t) = 1 - (1-\xi(t^*))\exp[-(t-t^*)/\tau_h]$ and converging to $\xi = 1$ with decay rate $1/\tau_h$. Both subsystems are first-order linear with strictly positive decay rates, so the post-arrest equilibrium $\boldsymbol{\chi} = \mathbf{0}$, $\xi = 1$ is reached asymptotically, with the two timescales τ_{rec} and τ_h independent of pre-arrest history. The arrested state acts as an energy sink: the kinematic hardening energy $\frac{1}{2c}\|\boldsymbol{\chi}\|^2$ is dissipated through the static recovery channel $\mathcal{D}_{\mathrm{stat}} = \|\boldsymbol{\chi}\|^2/(c\,\tau_{\mathrm{rec}})$ identified in Section 2.4, while ξ approaches its capacity-limited equilibrium through the postulated kinetics.

The foregoing analysis establishes asymptotic stability of flow arrest under sustained constant applied stress; perturbations to the applied stress are addressed implicitly in the kinematic argument of (31)–(39), where $\dot{\Sigma}_{\mathrm{eq}}$ is computed under the constant-load hypothesis.

3.3. Kinematic Hardening Acceleration Effect

Kinematic hardening not only contributes to flow arrest but accelerates its occurrence. To establish a baseline, consider first the case without kinematic hardening ($\chi \equiv 0$). The arrest condition then takes the form

$$\sigma_{\mathrm{eq}} = \sigma_Y\left(t_0^*\right) \tag{40}$$

where t_0^* denotes the arrest time in the absence of back stress. Substituting the threshold evolution (11) furnishes

$$\sigma_{\mathrm{eq}} = \sigma_{Y0} + \Delta\sigma_Y\left(1 - e^{-t_0^*/\tau_h}\right) \tag{41}$$

Solving for the arrest time, we obtain

$$t_0^* = -\tau_h \ln\left(1 - \frac{\sigma_{\mathrm{eq}} - \sigma_{Y0}}{\Delta\sigma_Y}\right) = -\tau_h \ln\left(\frac{\sigma_{Y\infty} - \sigma_{\mathrm{eq}}}{\Delta\sigma_Y}\right) \tag{42}$$

In dimensionless form this becomes

$$\frac{t_0^*}{\tau_h} = -\ln\left(1 - \frac{\Lambda - 1}{\Gamma}\right) \tag{43}$$

This solution exists and is finite ($0 < t_0^* < \infty$) precisely when $0 < (\Lambda-1)/\Gamma < 1$, i.e. when $1 < \Lambda < 1 + \Gamma$, which recovers the Regime II condition established in Section 3.1.

In view of (31), when kinematic hardening is present the arrest condition becomes $\sigma_{\mathrm{eq}} - \chi_{\mathrm{eq}}(t^*) = \sigma_Y(t^*)$. Because $\chi_{\mathrm{eq}}(t^*) > 0$, the threshold stress required at arrest is smaller than in the baseline case, $\sigma_Y(t^*) = \sigma_{\mathrm{eq}} - \chi_{\mathrm{eq}}(t^*) < \sigma_{\mathrm{eq}} = \sigma_Y(t_0^*)$. From the monotonicity of the threshold evolution (11), it follows that

$$t^* < t_0^* \tag{44}$$

Kinematic hardening hence accelerates flow arrest strictly ($t^* < t_0^*$).

To quantify the acceleration, substituting (11) into the arrest condition with back stress included and isolating the exponential factor gives the implicit relation for t^*,

$$t^* = -\tau_h \ln\left(\frac{\sigma_{Y\infty} - \sigma_{\mathrm{eq}} + \chi_{\mathrm{eq}}(t^*)}{\Delta\sigma_Y}\right) \tag{45}$$

Equation (45) is implicit in t^* because $\chi_{\mathrm{eq}}(t^*)$ itself depends on the arrest time through the back-stress evolution. In the regime $\tau_{\mathrm{rec}} \gg \tau_h$ relevant to Section 4, the back stress saturates on a timescale much shorter than the arrest time, so that $\chi_{\mathrm{eq}}(t^*) \to \chi_{\mathrm{sat}} = c/\kappa$ and (45) reduces to the explicit form used in (47).

The ratio of arrest times is then

$$\frac{t^*}{t_0^*} = \frac{\ln\left[\Delta\sigma_Y / \left(\sigma_{Y\infty} - \sigma_{\mathrm{eq}} + \chi_{\mathrm{eq}}\right)\right]}{\ln\left[\Delta\sigma_Y / \left(\sigma_{Y\infty} - \sigma_{\mathrm{eq}}\right)\right]} < 1 \tag{46}$$

The strict inequality holds because $\chi_{\mathrm{eq}} > 0$ makes the argument of the logarithm in the numerator smaller than that in the denominator. In the limit of small back stress ($\chi_{\mathrm{eq}} \ll \sigma_{Y\infty} - \sigma_{\mathrm{eq}}$), expansion of (46) shows the relative acceleration is proportional to χ_{eq} and inversely proportional to the overstress margin $\sigma_{Y\infty} - \sigma_{\mathrm{eq}}$.

When the back stress reaches its saturation value ($\chi_{\mathrm{eq}} \to \chi_{\mathrm{sat}} = c/\kappa$), the acceleration is greatest and the ratio attains its minimum value

$$\frac{t_{\min}^*}{t_0^*} = \frac{\ln\left[\Delta\sigma_Y / \left(\sigma_{Y\infty} - \sigma_{\mathrm{eq}} + c/\kappa\right)\right]}{\ln\left[\Delta\sigma_Y / \left(\sigma_{Y\infty} - \sigma_{\mathrm{eq}}\right)\right]} \tag{47}$$

The magnitude of the acceleration depends on the dimensionless ratio $c/(\kappa\,\Delta\sigma_Y)$ and on the position within Regime II. The fractional reduction $1 - t^*/t_0^*$ vanishes at the lower regime boundary ($\Lambda \to 1$), where the brief flow duration keeps $\chi_{\mathrm{eq}}(t^*)$ small, and grows monotonically as Λ increases; at the upper regime boundary ($\Lambda \to 1 + \Gamma$), t_0^* diverges while t^* asymptotes to the finite value $\tau_h \ln\left(\Delta\sigma_Y/\chi_{\mathrm{eq}}(t^*)\right)$, so the fractional reduction approaches unity. The actual acceleration for a given trajectory is bounded above by the saturation value (47), because $\chi_{\mathrm{eq}}(t^*) < c/\kappa$ when arrest occurs before back-stress saturation; the applicability of this acceleration to the material system studied here is discussed in Section 4. Physically, the back stress provides immediate resistance that complements the slower threshold evolution. Whereas σ_Y requires a time of order τ_h to approach saturation, the back stress develops rapidly during the initial flow transient; this early resistance permits arrest at a lower threshold value and hence at an earlier time. The yield surface translation and the resulting tension–compression asymmetry are illustrated in Figure 6 for three representative load ratios.

Figure 6 shows the mechanical consequences of kinematic hardening in stress space. During loading (panel a), the yield surface translates in the direction of the applied stress by an amount equal to the current back stress; the translation increases with Λ because higher stress levels produce faster inelastic strain accumulation and consequently faster back-stress growth. Upon unloading to zero stress (panel b), the translated surfaces show that the reverse yield stress — the compressive stress required to reinitiate flow — is reduced by twice the back stress, producing the Bauschinger effect. In panel (c), the back-stress trajectories follow the Armstrong–Frederick saturation dynamics; the continuous-flow case ($\Lambda = 1.80$) approaches the saturation plateau $\chi_{\mathrm{sat}} = c/\kappa$, while the arrested cases ($\Lambda = 1.20$ and 1.50) freeze at sub-saturation values when flow ceases, with the higher-Λ case freezing closer to saturation because the longer transient permits more back-stress accumulation before arrest. The tension–compression asymmetry quantified in panel (d) grows with Λ because the back stress at the evaluation time increases with the accumulated inelastic strain; this asymmetry is a prediction of the constitutive framework and would be absent in a purely isotropic hardening model.

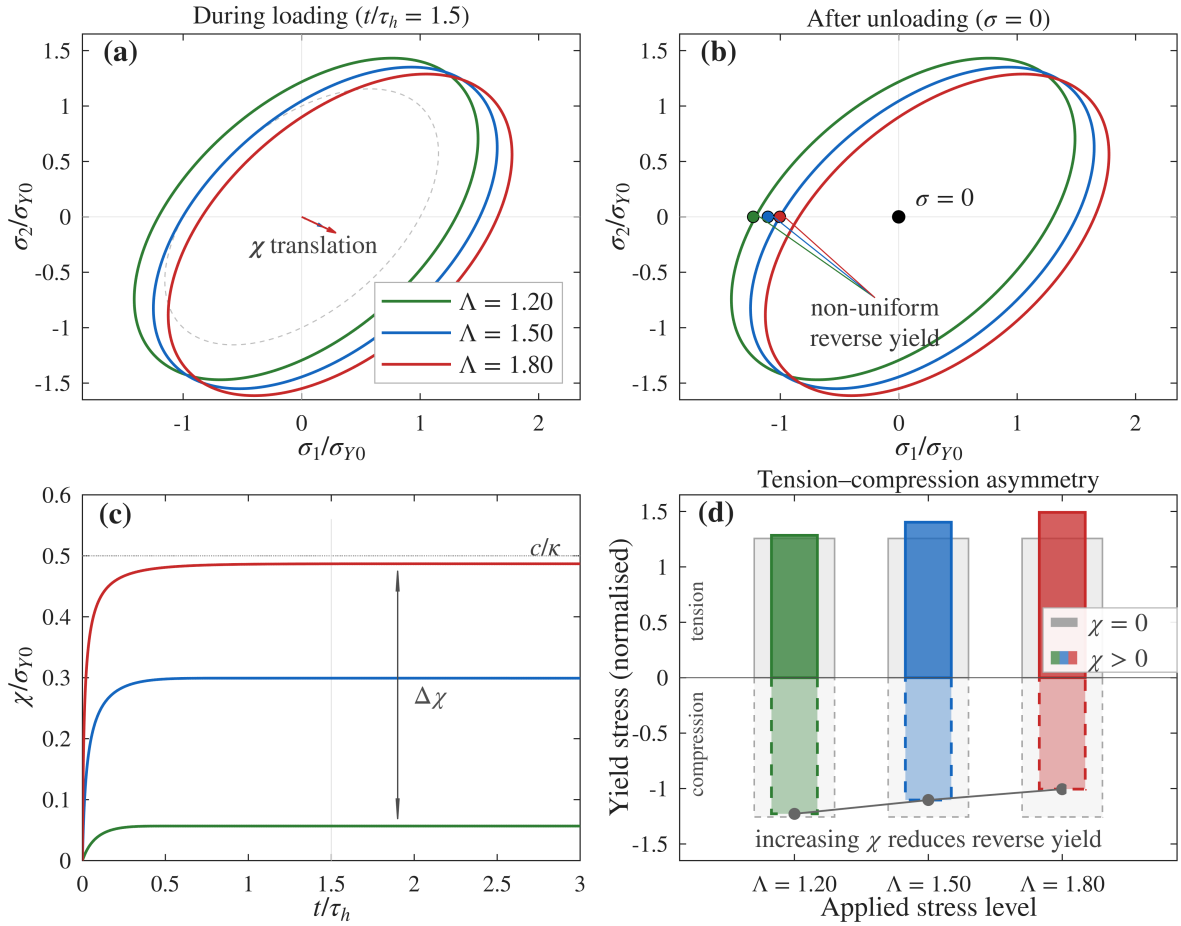

Figure 6: Yield surface evolution under kinematic hardening at three load ratios ($\Lambda = 1.20, 1.50, 1.80$): (a) translated von Mises surfaces during loading at $t/\tau_h = 1.5$, showing χ_{eq}-induced translation; (b) after unloading to $\sigma = 0$, showing non-uniform reverse yield points; (c) back-stress time histories $\chi_{\text{eq}}(t)/\sigma_{Y0}$, showing approach to saturation at c/κ for the continuous-flow case ($\Lambda = 1.80$) and frozen sub-saturation values for the arrested cases ($\Lambda = 1.20$ and 1.50); (d) tension–compression asymmetry bar chart showing that increasing χ_{eq} reduces reverse yield stress (Bauschinger effect).

3.4. Structural Results

The competitive-dynamics analysis of Sections 3.1–3.3 was carried out for the first-order exponential evolution kinetics of (10). Two structural questions remain. First, whether the constitutive class lacking a time-evolving threshold can reproduce the calibration outcome of the full framework, or whether the time-evolving threshold is required by the data. Second, whether the three-regime classification and the arrest-stability result are tied to the chosen first-order kinetics, or whether they extend to any monotonic, bounded threshold evolution.

Proposition 1 (Model discrimination). Let $\mathcal{M}_0$ denote the constitutive class consisting of a constant threshold $\sigma_Y(t) \equiv \sigma_{Y0}$, the Armstrong–Frederick kinematic hardening law (17) with parameters $(c, \kappa, \tau_{\mathrm{rec}})$, and the Perzyna flow rule (16). Consider a material for which (i) the asymptotic threshold strictly exceeds the initial threshold, $\sigma_{Y\infty} > \sigma_{Y0}$, and (ii) the applied stress exceeds the sum of initial threshold and saturation back stress, $\sigma_{\mathrm{eq}} > \sigma_{Y0} + \chi_{\mathrm{sat}}$, with χ_{sat} the equivalent saturation back stress independently determined (in the present illustration, from the back-stress test described in Section 4.1; any equivalent unloading-and-relaxation protocol would serve). No constant σ_{Y0} together with any choice of $(\eta, n, c, \kappa, \tau_{\mathrm{rec}})$ reproduces, with a single parameter set, both the measured saturation back stress $\chi_{\mathrm{sat}} = c/\kappa$ and the long-time deceleration of inelastic strain observed in the creep histories. A time-evolving threshold $\sigma_Y(t)$ is necessary as an independent internal state variable.

The proposition formalises the empirical motivation for the time-evolving threshold introduced in Section 2.2; its physical instantiation is taken up in the calibration discussion of Section 4.4. The structural argument runs as follows.

Under the loading conditions of the back-stress test, $\dot{p}\,\tau_{\mathrm{rec}} \gg 1$, so the saturation form (18) reduces to $\chi_{\mathrm{sat}} = c/\kappa$; the back-stress test therefore fixes the ratio c/κ in $\mathcal{M}_0$. The back stress in $\mathcal{M}_0$ is bounded above by this ratio for all t. To see this, the scalar reduction of (17) along the loading direction reads $\dot{\chi} = c\,\dot{p} - \kappa\chi\,\dot{p} - \chi/\tau_{\mathrm{rec}}$; evaluating at $\chi = c/\kappa$ gives

$$\dot{\chi}\big|_{\chi=c/\kappa} = c\,\dot{p} - \kappa \cdot \frac{c}{\kappa}\,\dot{p} - \frac{c/\kappa}{\tau_{\mathrm{rec}}} = -\frac{c}{\kappa\,\tau_{\mathrm{rec}}} < 0 \tag{48}$$

so $\chi = c/\kappa$ acts as a strict upper barrier. Starting from virgin material with $\chi(0) = 0$, the trajectory satisfies $\chi(t) < c/\kappa$ for all $t \geq 0$, independently of the value of τ_{rec} — static recovery cannot relax the bound; it only tightens it.

Combining this bound with condition (ii), the overstress in $\mathcal{M}_0$ satisfies

$$\Sigma_{\mathrm{eq}}(t) - \sigma_{Y0} = \sigma_{\mathrm{eq}} - \chi(t) - \sigma_{Y0} > \sigma_{\mathrm{eq}} - \chi_{\mathrm{sat}} - \sigma_{Y0} =: \delta > 0 \tag{49}$$

with δ a uniform positive lower bound on the overstress. The Perzyna flow rule (14) with constant threshold σ_{Y0} then gives $\dot{p} \geq (1/\eta)(\delta/\sigma_0)^n$ uniformly in t, and the accumulated inelastic strain grows at least linearly, $p(t) \geq (\delta/\sigma_0)^n\, t/\eta$. No arrest is possible within $\mathcal{M}_0$. The argument extends to multi-component Chaboche–Armstrong–Frederick formulations by replacing c/κ with the total saturation $\sum_i c_i/\kappa_i$: the uniform bound on $\chi(t)$ and the strict inequality on $\dot{p}$ are preserved.

The only parameter freedom that could alter this conclusion would be to raise c/κ above the independently measured value, which the constraint excludes. The argument is independent of whether the evolving-threshold model itself achieves strict arrest at the prescribed stress. When $\sigma_{Y\infty} + \chi_{\mathrm{sat}} > \sigma_{\mathrm{eq}}$ the contrast appears as arrest within the evolving-threshold model versus indefinite linear accumulation under $\mathcal{M}_0$; when $\sigma_{Y\infty} + \chi_{\mathrm{sat}} < \sigma_{\mathrm{eq}}$ — the regime occupied by the calibrated instance of Section 4.4 — the contrast appears as a decelerating creep rate under the evolving-threshold model, as $\sigma_Y(t)$ grows toward $\sigma_{Y\infty}$ and progressively reduces the overstress, versus an at-least-linearly accumulating strain under $\mathcal{M}_0$. The discrimination therefore rests on the time evolution of $\dot{p}$, not on the existence of finite arrest. Condition (i) implies that the threshold evolution is non-trivial; condition (ii) implies that $\mathcal{M}_0$ admits no static equilibrium. An independent χ_{sat} measurement — in the present illustration, that supplied by the back-stress test of Section 4.1 — furnishes the experimental obstruction to a constant-threshold description in any material satisfying (i) and (ii).

In plain state-variable terms, classical kinematic hardening of the Chaboche–Armstrong–Frederick type is a strain-history theory: time enters the back stress $\chi(t)$ only through the accumulated inelastic strain $p(t)$, so the entire memory of the loading history is carried by a single tensor whose evolution is driven by $\dot{p}$. The autonomous threshold $\sigma_Y(t)$ introduced in Section 2.2 adds an independent time-driven channel — an ingredient in the overstress that evolves with physical time, decoupled from strain history, and continues to evolve under $\dot{p} = 0$.

Proposition 2 (Regime invariance under kinetic generalisation). Let $\sigma_Y : [0, \infty) \to \mathbb{R}_+$ be any continuously differentiable, monotonically non-decreasing function satisfying $\sigma_Y(0) = \sigma_{Y0}$ and $\sigma_Y(t) \to \sigma_{Y\infty} < \infty$ as $t \to \infty$. Substituting $\sigma_Y(t)$ for the exponential form (11) in the flow rule (16), with the hardening capacity redefined as $\Gamma = (\sigma_{Y\infty} - \sigma_{Y0})/\sigma_{Y0}$, the three-regime classification of Section 3.1, in the form of its necessary-condition boundaries — Regime I ($\Lambda < 1$), Regime II ($1 < \Lambda < 1 + \Gamma$), and Regime III ($\Lambda > 1 + \Gamma$) — remains valid, and the asymptotic stability of flow arrest established in Section 3.2 is preserved. The arrest-time prediction (43), by contrast, depends on the specific kinetic form.

The argument proceeds in three parts: the regime boundaries, the asymptotic stability of arrest, and the kinetics-dependence of the arrest time.

For Regime I ($\Lambda < 1$), virgin initial conditions give $\chi(0) = 0$ and $\Sigma_{\text{eq}}(0) = \sigma_{\text{eq}} < \sigma_{Y0} = \sigma_Y(0)$, so the Macaulay bracket in (14) yields $\dot{p} = 0$. With $\dot{p} = 0$, the back-stress evolution (17) reduces to $\dot{\boldsymbol{\chi}} = -\boldsymbol{\chi}/\tau_{\text{rec}}$, decaying exponentially from $\boldsymbol{\chi}(0) = 0$, so $\boldsymbol{\chi}(t) \equiv 0$. Monotonicity of σ_Y then yields $\sigma_Y(t) \geq \sigma_{Y0} > \sigma_{\text{eq}}$; the Macaulay bracket remains zero, and no flow ever initiates. For Regime II ($1 < \Lambda < 1 + \Gamma$), at $t = 0$ one has $\Sigma_{\text{eq}}(0) - \sigma_Y(0) > 0$, so $\dot{p} > 0$ and flow initiates; since $\sigma_Y(t) \to \sigma_{Y\infty} > \sigma_{\text{eq}}$ by hypothesis, the resistance $\mathcal{R}(t) = \sigma_Y(t) + \chi(t)$ exceeds σ_{eq} at some finite t^* by continuity, regardless of the path taken between the endpoints. For Regime III ($\Lambda > 1 + \Gamma$), $\sigma_{\text{eq}} > \sigma_{Y\infty}$, and the necessary-condition boundary at $\Lambda = 1 + \Gamma$ retains its meaning of "applied stress exceeds the asymptotic threshold". The endpoint values $\mathcal{R}(0) = \sigma_{Y0}$ and $\sup_t \mathcal{R}(t) \leq \sigma_{Y\infty} + c/\kappa$ depend on σ_Y only through σ_{Y0} and $\sigma_{Y\infty}$, so both boundaries are kinetics-independent.

For the asymptotic stability of arrest, the direct integration argument of Section 3.2 carries through verbatim, since neither subsystem depends on the kinetic form of $\sigma_Y(t)$. The back-stress equation at arrest reduces to $\dot{\boldsymbol{\chi}} = -\boldsymbol{\chi}/\tau_{\text{rec}}$ regardless of $\sigma_Y(t)$, so $\boldsymbol{\chi}(t) \to \mathbf{0}$ exponentially with timescale τ_{rec}. Re-parametrising the threshold via $\xi(t) := [\sigma_Y(t) - \sigma_{Y0}]/\Delta\sigma_Y$ defines a mapping $\xi : [0, \infty) \to [0, 1]$ with $\xi(0) = 0$, $\xi(t) \to 1$, and $\dot{\xi} \geq 0$ for any monotonically non-decreasing $\sigma_Y(t)$; the boundedness hypothesis guarantees $\xi \to 1$. The asymptotic stability conclusion of Section 3.2 is therefore preserved.

The arrest-time prediction is, by contrast, kinetics-specific. The condition $\sigma_{\text{eq}} - \sigma_Y(t^*) - \chi(t^*) = 0$ requires integrating $\sigma_Y(t)$ against $\chi(t)$, both of which feed back into $\dot{p}$; the result is the inverse function of the resulting coupled system. For the exponential form (11), this integration yields (43); for other monotone bounded kinetics, t^* admits no kinetics-independent closed form.

The propositions separate the structural content of the framework — regime boundaries, stability of arrest, and the experimental obstruction to a constant-threshold description — from the kinetic content of the first-order evolution law adopted in Section 2.2. The exponential form (11) is sufficient for the calibrated instance of Section 4 but is not necessary for the structural results, and threshold-evolution kinetics derived from richer microstructural models may be substituted without re-deriving the regime analysis.

4. Empirical Illustration

The framework of Sections 2–3 is now calibrated to AA7050-T6 aluminium alloy at 174 °C using data from the back-stress test [35], described in Section 4.1. For uniaxial loading at constant stress, the general tensor flow rule (16) and back-stress evolution (17) reduce to the coupled scalar system

$$\frac{d\varepsilon^{\text{in}}}{dt} = \frac{1}{\eta}\left\langle \frac{\sigma - \chi - \sigma_Y(t)}{\sigma_0} \right\rangle^n, \qquad \frac{d\chi}{dt} = c\frac{d\varepsilon^{\text{in}}}{dt} - \kappa\chi\left|\frac{d\varepsilon^{\text{in}}}{dt}\right| - \frac{\chi}{\tau_{\text{rec}}}, \tag{50}$$

which serves as the forward model throughout the calibration.

4.1. Experimental Programme

The back-stress test provides independent access to inelastic strain and back stress. The loading phase furnishes inelastic strain histories; the post-unloading phase, in which the specimen is held at constant strain after unloading, provides a direct back-stress measurement as the applied stress relaxes to the residual internal stress. Tests were conducted at 174 ± 1 °C under uniaxial tension, with strain measured continuously by contact extensometry.

In each test, the specimen is loaded at 8 MPa/s to the target stress level and held at constant stress for a prescribed duration. The rapid loading rate minimises inelastic strain accumulation during the ramp, so that the creep holding

phase begins with negligible pre-strain. At the calibrated parameters of Section 4.3, the inelastic strain accumulated over the 17–20 s loading ramp is below 4×10^{-6} — three orders of magnitude smaller than the typical holding-phase strain. Tests were conducted at three stress levels — 137.5, 150, and 162.5 MPa — for holding durations of 5 min, 10 min, 30 min, 1, 2, 4, 6, and 8 hours; each combination requires a separate specimen, because the test is destructive. For calibration of the creep response, only the 8-hour holding data at all three stress levels are used, since these provide the longest observation window over which the competitive hardening dynamics can be resolved. The inelastic strain $\varepsilon^{\text{in}}(t)$ is the difference between the measured total strain during the constant-stress holding phase and the elastic component σ/E, where $E = 65.2$ GPa denotes the Young's modulus as determined from the unloading slope.

The back-stress test quantifies the internal stresses responsible for anelastic recovery. Existing methods for back-stress measurement — incremental unloading [2], strain transient dip [13], and stress change tests — determine the back stress at a single instant by perturbing the loading condition and observing the transient response. In the back-stress test, a specimen is crept at constant stress for a prescribed duration and then unloaded to zero stress, at which point the strain is held constant by the testing machine. Under this strain-constrained condition, the back stress manifests as a measurable stress that develops in the specimen and eventually saturates, giving a direct measurement of the back stress present at the end of the creep hold period.

The saturation back stress χ_{sat} is approximately independent of the applied stress level; it varies only with creep hold duration. This stress-independence is consistent with the Armstrong–Frederick kinematic hardening model adopted in Section 2, for which the theoretical saturation value $\chi_{\text{sat}} = c/\kappa$ is a material constant. The data used for calibration are the discrete saturation back-stress values $\chi_{\text{sat}}\left(t_{\text{creep}}\right)$ extracted from each test, which together trace the evolution of back stress with creep hold time. The complete test sequences at 150 MPa for all hold durations are displayed as a three-dimensional waterfall in Figure 7.

Two features of the data displayed in Figure 7 directly constrain the constitutive model. The back-stress rise curves (orange segments) show an initial rapid increase followed by saturation at a plateau value that grows with hold duration up to approximately 4 h, beyond which further holding produces no additional back stress. This saturation corresponds to the Armstrong–Frederick dynamic recovery term $(-\kappa\chi\dot{p})$ in Eq. (17), which limits the back stress to $\chi_{\text{sat}} = c/\kappa$ regardless of the total accumulated strain. In addition, the plateau values are approximately independent of the applied stress level — a feature confirmed across all three stress levels in the full test matrix — consistent with the theoretical prediction that χ_{sat} is a material constant rather than a function of the applied loading.

4.2. Calibration Procedure

The uniaxial specialisation of the constitutive framework involves seven fitted parameters — σ_{Y0}, $\Delta\sigma_Y$, τ_h, η, n, c, and κ — and two fixed constants: the reference stress $\sigma_0 = 1$ MPa (a normalisation constant degenerate with η) and the static recovery time $\tau_{\text{rec}} = 10^6$ s.

The reference stress σ_0 cannot be determined independently, because the flow rule contains the compound quantity $\eta \cdot \sigma_0^n$; only this product is identifiable from data. The static recovery time τ_{rec} significantly exceeds the observation window, and the data show no visible back-stress decay after saturation; τ_{rec} is therefore fixed at 10^6 s throughout.

The experimental data impose physical constraints that restrict the parameter space before fitting begins. At $t = 0$, the back stress is zero and the threshold stress is at its initial value σ_{Y0}. The flow rule then reduces to $\dot{\varepsilon}^{\text{in}}(0) = (1/\eta)\left[(\sigma - \sigma_{Y0})/\sigma_0\right]^n$, and the ratio of any two initial rates eliminates η, giving

$$\frac{\dot{\varepsilon}_0^{\text{in}}(\sigma_1)}{\dot{\varepsilon}_0^{\text{in}}(\sigma_2)} = \left(\frac{\sigma_1 - \sigma_{Y0}}{\sigma_2 - \sigma_{Y0}}\right)^n \tag{51}$$

Two such ratios from three stress levels furnish two equations in two unknowns (n, σ_{Y0}). Once these are determined, η follows from any single initial rate. The saturation back stress $\chi_{\text{sat}} \approx c/\kappa$ is read directly from the plateau of the back-stress test data, so that the ratio c/κ is constrained before the full optimisation begins.

The calibration accordingly proceeds in three stages: the initial-rate ratios (51) first fix n, σ_{Y0}, and η; the back-stress test saturation plateau then fixes c/κ; and all seven parameters are refined simultaneously by nonlinear least-squares minimisation, initialised from these prior estimates. The parameter σ_{Y0} is constrained to be non-negative on physical grounds.

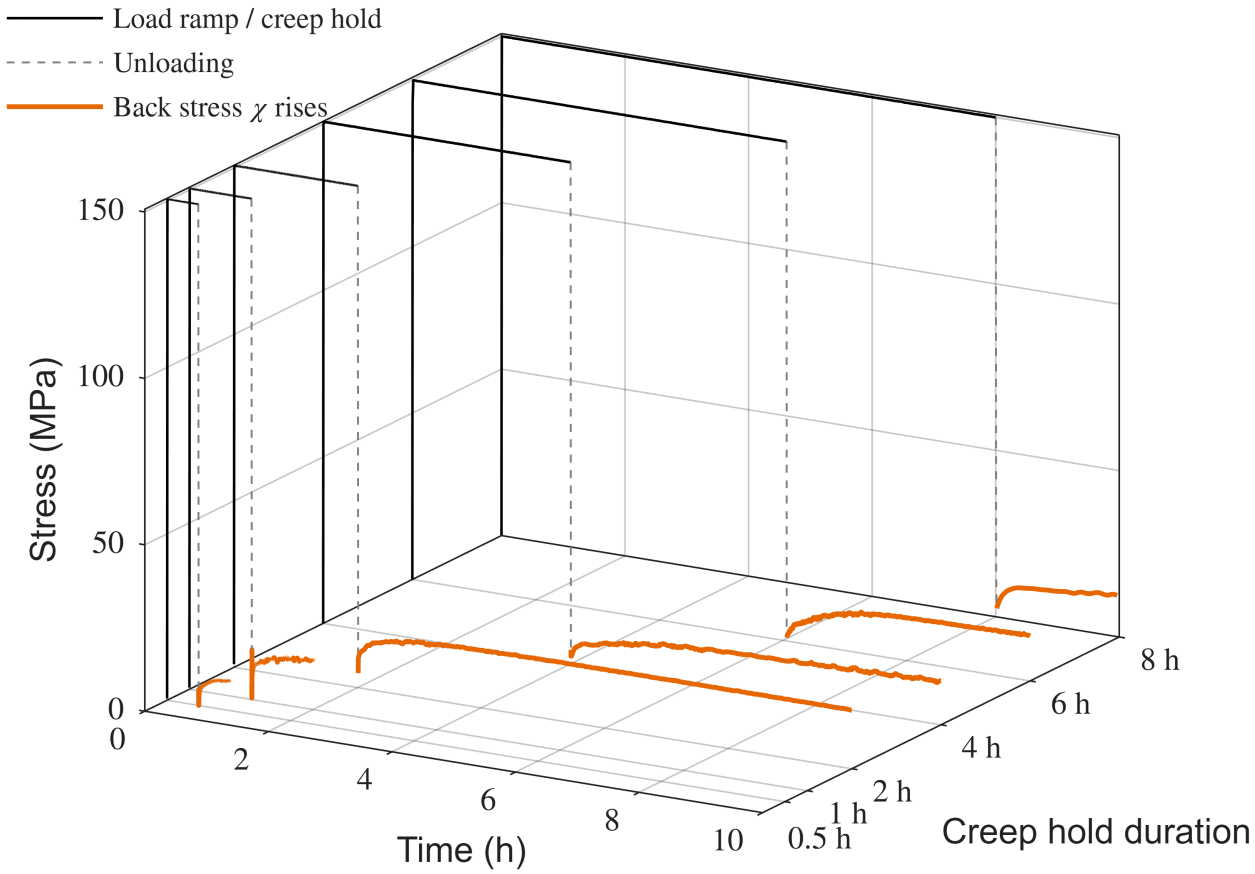

Figure 7: Back-stress measurements on AA7050-T6 at 150 MPa and 174 °C, illustrating the back-stress evolution behaviour the framework is designed to capture in viscoplastic materials with time-evolving threshold stress. Each curve represents a complete test sequence — load ramp (black), unloading (dashed), and back-stress rise phase (orange) — for creep hold durations from 0.5 h to 8 h.

The seven parameters are fitted simultaneously to both datasets by nonlinear least-squares minimisation (Levenberg–Marquardt via MATLAB `lsqnonlin`) of the combined cost function

$$\mathcal{J}(\mathbf{p}) = \sum_{k=1}^{3} \left\| \frac{\varepsilon^{\mathrm{in}}_{\mathrm{model}}(t;\sigma_k,\mathbf{p}) - \varepsilon^{\mathrm{in}}_{\mathrm{exp}}(t;\sigma_k)}{\varepsilon^{\mathrm{in,max}}_{\mathrm{exp}}(\sigma_k)} \right\|^2 + w_\chi \sum_{k=1}^{3} \sum_{j} \left(\frac{\chi_{\mathrm{model}}\left(t_j;\sigma_k,\mathbf{p}\right) - \chi_{\mathrm{exp}}\left(t_j;\sigma_k\right)}{\chi_{\mathrm{sat}}} \right)^2 \tag{52}$$

where $\mathbf{p} = (\sigma_{Y0}, \Delta\sigma_Y, \tau_h, \eta, n, c, \kappa)$, the first sum runs over the three creep stress levels with continuous time series, and the second sum runs over the discrete back-stress measurements. The forward model integrates the coupled ODE system (50) with `ode15s` at tolerance 10^{-10}. Each dataset is normalised by its characteristic scale — the maximum observed inelastic strain for the creep data, the saturation back stress for the back-stress data — and the weight w_χ is chosen so that neither dataset dominates the combined objective. Within the constrained subspace established above, three independent random restarts of the joint optimiser converge to the same parameter values within solver tolerance. The joint use of creep strain and back-stress data suppresses the parameter degeneracy that would otherwise affect a creep-only calibration of the back-stress kinetics.

4.3. Calibration Results

The calibrated parameters are listed in Table 2.

Table 2: Calibrated material parameters for AA7050-T6 at 174 °C.

Parameter	Symbol	Value	Unit
Initial threshold stress	σ_{Y0}	0	MPa
Threshold increment	$\Delta\sigma_Y$	86.7	MPa
Threshold time constant	τ_h	3552	s
Viscous resistance	η	5.42×10^9	s
Stress exponent	n	1.39	—
Back-stress modulus	c	7.18×10^4	MPa
Dynamic recovery coefficient	κ	4756	—
Reference stress (fixed)	σ_0	1	MPa
Static recovery time (fixed)	τ_{rec}	10^6	s

The calibrated model is compared against the experimental inelastic strain histories in Figure 8(a). The model reproduces the primary creep deceleration and the transition toward secondary creep at all three stress levels with a single parameter set. The mean RMSE across the three stress levels is 0.004% strain. The stress sensitivity is also reproduced, since the creep rate increases with applied stress in a manner consistent with the power-law flow rule. A slight over-prediction at 162.5 MPa in the late-time region (beyond 5 h) reflects the single-kinetics limitation of the exponential threshold-evolution function (11); the real precipitation process involves an early fast phase and a later slow phase that one time constant cannot resolve.

The back-stress evolution predicted by the calibrated model is compared against the discrete back-stress measurements in Figure 8(b). The model recovers both the rapid build-up during primary creep and the saturation toward $\chi_{\mathrm{sat}} = c/\kappa = 15.1$ MPa. The approximate stress-independence of χ_{sat} is likewise recovered; the three stress levels converge to similar saturation values, consistent with the Armstrong–Frederick structure in which χ_{sat} is a material constant. The mean RMSE across the three stress levels is 1.1 MPa. The back-stress data constrain the ratio c/κ but not the individual values; the individual magnitudes of c and κ are determined primarily by the rate of back-stress build-up observed in the creep data. The seven-parameter fit therefore reproduces both inelastic strain histories and back-stress saturation values with a single parameter set.

4.4. Discussion

The seven-parameter calibration produces a constitutive model that simultaneously reproduces two independent experimental datasets — creep strain histories and back-stress evolution from the back-stress test — at three stress levels with a single parameter set. Several observations merit discussion.

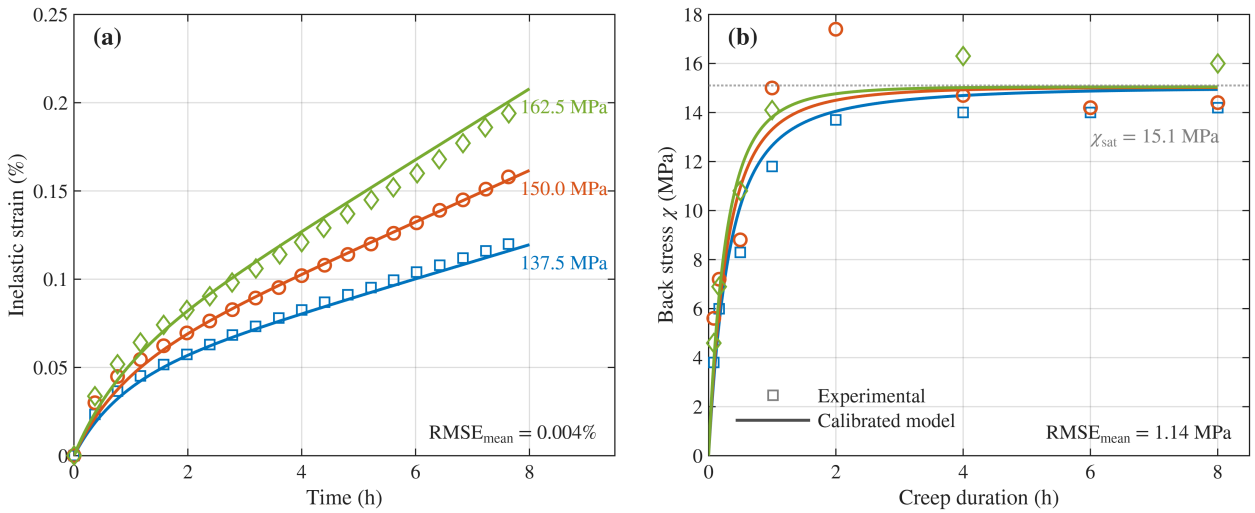

Figure 8: Application of the framework to AA7050-T6 at 174 °C: (a) inelastic creep strain histories at 137.5, 150 and 162.5 MPa with the calibrated ODE model (solid lines) and experimental data (markers); (b) back-stress evolution from the back-stress test (markers) with the calibrated ODE model (solid). The framework's predictive structure is illustrated on one viscoplastic material; the formulation itself is material-agnostic. Calibrated saturated back stress $\chi_{sat} \approx 15.1$ MPa.

The back-stress test provides the only direct experimental access to the back stress in this framework. Without it, the parameters c and κ would be determined indirectly from the curvature of the creep curves — a numerically ill-conditioned procedure, since χ enters the flow rule as a correction to the applied stress and its individual effect is difficult to distinguish from changes in σ_{Y0} or η; the back-stress data accordingly resolve this ambiguity through an independent measurement that constrains the back-stress subsystem.

With $\sigma_{Y0} = 0$, the asymptotic threshold $\sigma_{Y\infty} = \Delta\sigma_Y = 86.7$ MPa serves as the normalising stress (Remark, Section 3.1), giving the reduced load ratio $\Lambda_\infty = \sigma_{eq}/\sigma_{Y\infty}$. The initial-rate ratio (51) reduces to $(\sigma_1/\sigma_2)^n$, so the stress exponent n follows directly from the ratio of initial creep rates.

At 137.5 MPa ($\Lambda_\infty = 1.59$), 150 MPa ($\Lambda_\infty = 1.73$), and 162.5 MPa ($\Lambda_\infty = 1.87$), all three experimental stress levels lie well above the asymptotic threshold and are therefore in the continuous flow regime, consistent with the experimental creep curves, which show sustained creep throughout the 8-hour window without the strain plateau that would indicate arrest.

The present calibration contains no arrest-regime data, because all three stress levels lie well into the continuous flow regime ($\Lambda_\infty > 1.5$). Experimental verification of the arrest transition predicted by the framework (Sections 3.1–3.2) would require applied stresses below $\sigma_{Y\infty} = 86.7$ MPa — a regime accessible through stress relaxation or low-stress creep tests, which would also permit evaluation of the kinematic hardening acceleration ratio (46) and its saturation upper bound (47), neither of which the present calibration constrains.

The present calibration uses only the constant-stress holding phase, since post-unloading anelastic recovery requires a signed flow rule capable of reverse inelastic flow. The static recovery timescale τ_{rec} is likewise unidentifiable from the present dataset; its determination requires either much longer observation windows or controlled reverse-loading experiments.

5. Conclusions

A constitutive framework has been developed in which the threshold stress is governed by first-order microstructural kinetics and evolves with physical time independently of the accumulated inelastic strain. The back stress follows a modified Armstrong–Frederick evolution with static recovery, and the two subsystems are coupled through the Perzyna-type flow rule. Thermodynamic admissibility has been established for all admissible processes through the Clausius–Duhem inequality (Section 2.4).

The competition between time-driven threshold evolution and strain-driven kinematic hardening gives rise to three behavioural regimes — elastic, flow arrest, and continuous flow — classified by the dimensionless load ratio Λ and hardening capacity Γ (Section 3.1, Figure 5). Direct integration of the decoupled post-arrest evolution equations establishes that flow arrest is asymptotically stable, with explicit decay timescales τ_{rec} for the back stress and τ_h for the microstructural state variable. The analytical formula for the kinematic hardening acceleration effect (46) shows that back-stress development strictly reduces arrest time across the arrest regime, with the saturation upper bound (47) characterising in closed form the maximum possible reduction.

A structural no-go result establishes (Proposition 1 of Section 3.4) that within the constant-threshold Armstrong–Frederick class, no parameter choice reproduces both an independently measured saturation back stress and the long-time deceleration of inelastic strain observed in the creep histories; the time-evolving threshold is therefore necessary as an independent internal state variable for any material satisfying the two stated empirical conditions. The regime classification and arrest-stability results extend to any monotonic, bounded threshold kinetics (Proposition 2 of Section 3.4), so that the first-order exponential form adopted here is a calibration choice rather than a structural one.

A seven-parameter joint calibration of the two subsystems against data from the back-stress test [35] is reported in Section 4. The one-sided Macaulay bracket adopted here admits only forward inelastic flow; extension to anelastic recovery and the Bauschinger effect would require a signed flow rule.

Declaration of competing interest

The author declares that there are no known competing financial interests or personal relationships that could have appeared to influence the work reported in this paper.

Acknowledgments

This research was funded by the National Science and Technology Council (NSTC), Taiwan, under Grant No. 112-2221-E-027-118-. The experimental data reported in Section 4 were obtained at the Department of Mechanical Engineering, Imperial College London, as part of the author's doctoral research under the supervision of Prof. Jianguo Lin.

Declaration of generative AI and AI-assisted technologies in the manuscript preparation process

During the preparation of this work the author used Claude (Anthropic) to proofread and improve the language of the manuscript, and to assist in writing the code used to produce the figures. After using this tool, the author reviewed and edited the content as needed and takes full responsibility for the content of the published article.

References

[1] Zener, C., *Elasticity and anelasticity of metals*. 1948, Chicago, Illinois: University of Chicago Press.

[2] Gibeling, J.C. and W.D. Nix, *The description of elevated temperature deformation in terms of threshold stresses and back stresses: A review.* Materials Science and Engineering, 1980. **45**(2): p. 123–135.

[3] Sinha, N.K., *Viscous and delayed-elastic deformation during primary creep-using strain relaxation and recovery test.* Scripta Materialia, 2003. **48**(10): p. 1507–1512.

[4] Sinha, N.K. and S. Sinha, *High-temperature yield strength and its dependence on primary creep and recovery.* Materials Science and Engineering: A, 2011. **528**(16–17): p. 5366–5378.

[5] Gibeling, J.C. and W.D. Nix, *Observations of anelastic backflow following stress reductions during creep of pure metals.* Acta Metallurgica, 1981. **29**(10): p. 1769–1784.

[6] Li, D. and R.H. Wagoner, *The nature of yielding and anelasticity in metals.* Acta Materialia, 2021. **206**: p. 116625.

[7] Mughrabi, H., *Dislocation wall and cell structures and long-range internal stresses in deformed metal crystals.* Acta Metallurgica, 1983. **31**(9): p. 1367–1379.

[8] Zelenika, A., et al., *Observing formation and evolution of dislocation cells during plastic deformation.* Scientific Reports, 2025. **15**(1): p. 8655.

[9] Zirkle, T., T. Zhu, and D.L. McDowell, *Micromechanical crystal plasticity back stress evolution within FCC dislocation substructure.* International Journal of Plasticity, 2021. **146**: p. 103082.

[10] Čadek, J., *The back stress concept in power law creep of metals: A review.* Materials Science and Engineering, 1987. **94**: p. 79–92.

[11] Kassner, M.E., P. Geantil, and L.E. Levine, *Long range internal stresses in single-phase crystalline materials.* International Journal of Plasticity, 2013. **45**: p. 44–60.

[12] Chen, B., et al., *A review of the changes of internal state related to high temperature creep of polycrystalline metals and alloys.* International Materials Reviews, 2015. **60**(1): p. 1–29.

[13] Ahlquist, C.N. and W.D. Nix, *The measurement of internal stresses during creep of al and Al-Mg alloys.* Acta Metallurgica, 1971. **19**(4): p. 373–385.

[14] Chen, R., et al., *Hetero-deformation induced (HDI) stress measurement from the plastic dissipation in the hysteresis loops.* Materials Research Letters, 2025. **13**(3): p. 248–255.

[15] Perzyna, P., *Fundamental Problems in Viscoplasticity*, in *Advances in Applied Mechanics*, G.G. Chernyi, et al., Editors. 1966, Elsevier. p. 243–377.

[16] Chaboche, J.L., *Viscoplastic constitutive equations for the description of cyclic and anisotropic behaviour of metals.* Bulletin de l'Académie Polonaise des Sciences, Série des Sciences Techniques, 1977. **25**(1): p. 39–48.

[17] Chaboche, J.L., *A review of some plasticity and viscoplasticity constitutive theories.* International Journal of Plasticity, 2008. **24**(10): p. 1642–1693.

[18] Chaboche, J.L., *Time-independent constitutive theories for cyclic plasticity.* International Journal of Plasticity, 1986. **2**(2): p. 149–188.

[19] Meyer, K.A. and J. Ahlström, *The role of accumulated plasticity on yield surface evolution in pearlitic steel.* Mechanics of Materials, 2023. **179**: p. 104582.

[20] Deschamps, A. and Y. Bréchet, *Influence of predeformation and ageing of an Al–Zn–Mg alloy—II. Modeling of precipitation kinetics and yield stress.* Acta Materialia, 1998. **47**(1): p. 293–305.

[21] Seidman, D.N., E.A. Marquis, and D.C. Dunand, *Precipitation strengthening at ambient and elevated temperatures of heat-treatable Al(Sc) alloys.* Acta Materialia, 2002. **50**(16): p. 4021–4035.

[22] Fribourg, G., Y. Bréchet, A. Deschamps, and A. Simar, *Microstructure-based modelling of isotropic and kinematic strain hardening in a precipitation-hardened aluminium alloy.* Acta Materialia, 2011. **59**: p. 3621–3635.

[23] Ho, K.C., J. Lin, and T.A. Dean, *Constitutive modelling of primary creep for age forming an aluminium alloy.* Journal of Materials Processing Technology, 2004. **153–154**: p. 122–127.

[24] Dyson, B.F., *Microstructure based creep constitutive model for precipitation strengthened alloys: theory and application.* Materials Science and Technology, 2009. **25**(2): p. 213–220.

[25] Lemaitre, J. and J.-L. Chaboche, *Mechanics of Solid Materials*. 1990, Cambridge: Cambridge University Press.

[26] Prager, W., *A New Method of Analyzing Stresses and Strains in Work-Hardening Plastic Solids.* Journal of Applied Mechanics, 1956. **23**(4): p. 493–496.

[27] Frederick, C.O. and P.J. Armstrong, *A mathematical representation of the multiaxial Bauschinger effect.* Materials at High Temperatures, 2007. **24**(1): p. 1–26.

[28] Chaboche, J.L., *Constitutive equations for cyclic plasticity and cyclic viscoplasticity.* International Journal of Plasticity, 1989. **5**(3): p. 247–302.

[29] Coleman, B.D. and M.E. Gurtin, *Thermodynamics with Internal State Variables.* Journal of Chemical Physics, 1967. **47**: p. 597–613.

[30] Zhu, Y., et al., *Thermo-mechanically coupled cyclic elasto-viscoplastic constitutive model of metals: Theory and application.* International Journal of Plasticity, 2016. **79**: p. 111–152.

[31] Oppermann, P., R. Denzer, and A. Menzel, *A thermo-viscoplasticity model for metals over wide temperature ranges- application to case hardening steel.* Computational Mechanics, 2022. **69**(2): p. 541–563.

[32] Petryk, H., *Stability and constitutive inequalities in plasticity*, in *Non-Equilibrium Thermodynamics with Application to Solids*, W. Muschik (Ed.), CISM Courses and Lectures No. 336. 1993, Springer Vienna, p. 259–329.

[33] Nguyen, Q.S., *Bifurcation and stability in dissipative media (plasticity, friction, fracture).* Applied Mechanics Reviews, 1994. **47**(1): p. 1–31.

[34] Petryk, H., *Thermodynamic conditions for stability in materials with rate-independent dissipation.* Philosophical Transactions of the Royal Society A, 2005. **363**(1836): p. 2479–2515.

[35] Yang, Y.-L., *A study of inelastic/anelastic behaviour and springback of AA7050 alloy in creep age forming*, in *Mechanical Engineering*. 2017, Imperial College London: London.